universität wien

MASTERARBEIT

Titel der Masterarbeit

„Towards multiple measurements of a single Bose-Einstein condensate by coherent outcoupling “

verfasst von

Mira Maiwöger, BSc

angestrebter akademischer Grad

Master of Science (MSc.)

Wien, 2015

Studienkennzahl lt. Studienblatt:	A 066 876
Studienrichtung lt. Studienblatt:	Masterstudium Physik UG2002
Betreut von:	Univ. Prof. Dr. Hannes-Jörg Schmiedmayer

Abstract

This thesis deals with coherent output coupling as a method to probe the same cloud of ultracold atoms multiple times. We are especially interested in observing interference fringes formed by atoms output coupled from a Bose-Einstein condensate (BEC) confined in a double-well potential. Within this thesis output coupling from magnetic traps was studied with microwave- and radiofrequency radiation. Also, a laser system was built to output couple with two-photon Raman transitions. As our experiment uses magnetic traps with spatially inhomogeneous magnetic fields, the second-order Zeeman shift gives rise to an effective potential that acts as a magnetic lens and (de)focuses the transverse density profiles of the output coupled clouds. This effect prevents the observation of interference fringes from output coupled atoms. We expect to achieve this with the Raman laser system, based on the following two factors: First, we choose a spatial configuration of the two Raman laser beams such that photon-momentum is imparted onto the output coupled atoms. The atoms therefore leave the trapping region with strongly curved magnetic fields faster. Consequently, we expect the effect of the magnetic lens to be weaker. Second, we expect coupling strengths up to 1 MHz, which is three orders of magnitude stronger than what we could achieve with microwave output coupling. This enables us to output couple with short broadband pulses. Once we are able to perform phase measurements on a fraction of output coupled atoms we can use this system to investigate phase diffusion or the dynamics of the relative phase of BECs confined in double well potentials. Further we can use output coupling to study the quantum measurement back-action on the BEC and realize weak measurements on Bose-Einstein condensates.

Zusammenfassung

Die vorliegende Arbeit beschäftigt sich mit kohärentem Auskoppeln als Methode um mehrfach Messungen an demselben Bose-Einstein Kondensat (BEK) vorzunehmen. Von Interesse ist insbesondere die Beobachtung von Interferenzstreifen, geformt von wenigen Atomen, die aus einem Kondensat in einem Doppelmulden Potential ausgekoppelt wurden. Im Rahmen dieser Arbeit wurde kohärentes Auskopplen mithilfe von Radiofrequenz- und Mikrowellenstrahlung untersucht. Außerdem wurde ein Laser System angefertigt, das Auskoppeln mithilfe von zwei-Photonen Raman-Übergängen ermöglichen soll. Da unser Experiment Magnetfallen mit räumlich stark inhomogenen Magnetfeldern verwendet, führt der quadratische Zeeman-Effekt zu einem effektiven Potential, das ähnlich einer magnetische Linse die transversalen Dichteprofile der ausgekoppelten Atomwolken (de)fokussiert. Dieser Effekt verhindert bisher die Beobachtung von Interferenzstreifen in ausgekoppelten Atomwolken. Wir erwarten jedoch, dass dies mithilfe des neu angefertigten Raman Laser Systems gelingen kann, begründet duch die folgenden zwei Faktoren: Erstens wird durch die gewählte räumliche Konfiguration der beiden Raman-Laserstrahlen Photonen-Impuls auf die ausgekoppelten Atome übertragen. Die Atome verlassen die Fallenregion dadurch schneller. Wir erwarten, dass dies den Effekt der magnetischen Linse deutlich verringern könnte. Zweitens erwarten wir Kopplungsstärken bis zu 1 MHz, etwa 3 Größenordnungen stärker als wir mit Auskopplung durch Mikrowellenstrahlung erreichen konnten. Dies ermöglich die Auskopplung mit kurzen Breitband-Pulsen. Sobald es gelingt die relative Phase zweier BEK mithilfe von wenigen augekoppelten Atomen zu messen, kann dieses System beispielsweise zur Untersuchung von Phasendsiffusion oder der Dynamik der relativen Phase von BEK in Doppelmulden Potentialen verwendet werden. Ein weiteres Anwendungsgebiet ist die Untersuchung der Rückwirkung der Messung auf das BEK und die Umsetzung von schwachen Messungen an Bose-Einstein Kondensaten.

Contents

List of Figures

1 Introduction

The first experimental observation of Bose-Einstein condensation [1, 15] twenty years ago opened completely new possibilities for studying the properties of manybody quantum systems. It is now possible to design cold atom experiments to simulate other systems. Ultracold gases are used as quantum simulators to address questions associated with condensed matter physics, high energy physics or cosmology [24]. To give one example, neutral atoms in optical lattice potentials are used for quantum simulation of magnetic ordering (e.g [23, 57]). Another key application of Bose-Einstein condensates (BECs) is metrology and inertial sensing [14]. As atoms are sensitive to gravitational forces and accelerations, cold atoms are used as probes for inertial effects (among others) in atom interferometers. In a BEC all particles occupy the same single-particle quantum state which makes BECs a source of coherent matter waves analogous to a laser for light. The fundamental difference between a coherent state of photons and a coherent state of atoms is the presence of atom-atom interactions in the latter. These interactions lead to dephasing, which limits the coherence time and precision of a BEC based interferometer. On the other hand, the nonlinear nature of interparticle interactions provides a mechanism to create nonclassical states - squeezed atomic states with reduced fluctuations in some observable - which can provide a coherent atomic source for precision measurements with higher precision than can be achieved with classical input states [26]. These prospects make phase properties of BECs interesting to investigate on its own.

The achievement of Bose-Einstein condensation led to the developement of a variety of experimental tools and techniques to trap, coherently manipulate and image clouds of ultracold atoms [32, 43]. We now have the possibility to create BECs in small and compact setups, for example on atom chips [19, 60] which are microfabricated wire structures that produce the magnetic fields to trap and manipulate neutral atoms. Atoms can be detected to single-particle precision and good spatial resolution [11] which allows a precise measurement of atom numbers and enables the detection of correlations in quantum degenerate systems. Most information on BECs is inferred from images of the atom distribution. The atom distribution is either imaged after ballistic expansion in time of flight (tof) or in situ by dispersive imaging methods, like phase contrast imaging or dark-ground imaging. [32] When imaging in tof the entire cloud of atoms is dropped after switching off the trap and can only be imaged once in each experimental realization. In order to investigate the dynamics of properties that depend on initial conditions which are hard to control and reproduce precisely, one can either post-select the experimental data

or do multiple measurements on the same sample of ultracold atoms [22, 49]. Multiple probing schemes can for example be realized by changing the internal state of a small fraction of atoms such that they become untrapped and can be imaged in tof, while the atoms remaining in the trap can be imaged at a later point in time. While post-selecting the data naturally requires a large amount of data taking, multiple probing schemes are restricted by the measurement back-action on the quantum system.

This thesis documents the first steps towards the realization of multiple probing schemes on the Rubidium 2 (Rb2) experiment, an atomchip based experiment introduced in chapter 3 of this thesis (or see references [4, 9]). We want to access information about the same ultracold system several times by coupling part of the atoms to an untrapped state. The atoms will leave the trap and can be imaged before switching off the trap, releasing and imaging the remaining part of the BEC. The first goal is to implement a laser system to output couple atoms which allows to infer the relative phase from a fraction of atoms of a BEC confined in a doublewell potential, to investigate its phase evolution and the back-action of the output coupling process on the remaining part of the BEC.

Before giving an overview of the structure of this thesis I will give a brief review of phase measurements of a BEC and methods to output couple atoms from a BEC.

Phase measurement of a BEC

Interference of two independent BECs In 1997 the observation of interference between two ^{23}Na BECs [2] which were created independently, released from their trap and allowed to overlap in tof was a first demonstration of macroscopic coherence properties of BECs. Atoms in a three-dimensional BEC (at zero temperature) are in a coherent state described by a single wave function. The phase relation between two independently prepared condensates is established in the measurement process. As Javanainen and Wilkens phrase it [30]:

> [...] *a measurement looking for interference of two condensates will find the characteristic consequences of the phase, even if there is no phase in the initial state of the system.*

The spatial overlap of the two atomic clouds in tof provides the same mechanism as the recombination at a beamsplitter. Two independently prepared condensates will show a definite value for their phase difference ϕ due to their intrinsic coherence properties. In each experimental run however, the phase differences will be completely randomly distributed [13] and averaging over many experimental realization causes the fringe contrast to wash out.

When performing successive phase measurements on the same pair of condensates, the first measurement establishes a fixed phase relation between the two and the subsequent

measurements show correlations in the relative phase of the condensates. This has been shown in an experiment in 2005 [49] which continuously probed the relative phase of two independent BECs confined in optical doublewell potentials by stimulated light scattering. The experiment also showed that the evolution of the relative phase can be controlled by applying an energy offset ΔE for a time Δt. After a measurement that establishes the fixed phase relation between the initially independent condensates, their relative phase ϕ evolves linearly as $\mathrm{d}\phi/\mathrm{d}t = \Delta E/h$, where h is Planck's constant.

To understand how a fixed phase relation between two BECs establishes, we have to dig a bit deeper: Phase difference ϕ and number difference n are canonical conjugate observables, they obey Heisenberg's uncertainty relation $\Delta n \Delta\phi \geq 1$, where Δn denotes the variance of the number difference and $\Delta\phi$ the variance of the relative phase. If we know the number difference between two BECs precisely, the relative phase is completely random. We still can observe interference between two independent BECs in each experimental shot as described above, because of the overlap of their wavefunctions in tof. In the overlap region we cannot distinguish whether a single atom originates from one or the other BEC. This results in an uncertainty in the number difference and allows the establishment of a fixed phase relation between the two BECs. In the case of two independently prepared BECs, we can however not assume that their phase relation exists prior to its observation.

Interference of coherently split BECs Coherent splitting of a BEC allows to create two BECs with a well defined initial relative phase. This can be done by adiabatically splitting a magnetic trap on an atom chip into a doublewell potential by means of radiofrequency (RF) dressing [52]. If the doublewell potential has a well spacing and barrier height such that atoms can tunnel between the two wells, the BECs show a fixed relative phase, i.e the measured phase difference is narrowly distributed. In reference [29], the interference of two coherently split and of two independently created BECs is compared for the same trapping potentials. While the first show a narrow distribution of the relative phase, in the latter the relative phase is randomly distributed.

Phase diffusion Fluctuations in the number of atoms in a BEC lead to decoherence. As discussed above, for a BEC with a well defined atom number, its phase is indeterminate. In order to have a well determined phase, a BEC must be in superposition of states with different atom number. As the mean field energy of a trapped BEC increases with the atom number N, the different number states have different energy and evolve at a different rate. They get out of phase, which limits the accuracy of a BEC interferometer. The timescale on which this dephasing occurs is given by the phase diffusion rate which can be estimated by [14]

$$R_\phi = \frac{1}{\hbar}\frac{\mathrm{d}\mu}{\mathrm{d}N}\Delta N$$

where μ is the chemical potential of the BEC. The phase diffusion rate is lower for number

squeezed states, states with reduced fluctuations in the atom number difference compared to coherent states. In reference [5], the implementation of a Mach-Zehnder type interferometer for BECs split in doublewell potentials at the Rb2 setup is presented. It is shown that the coherently split BECs exhibit reduced number fluctuations together with coherence times longer than expected for a coherent state. The creation of such spin squeezed states is currently under investigation.

Output coupling from a BEC: atom lasers

We already stated that the coherence properties of a BEC resemble those of an optical laser, with the key difference of the presence of interparticle interactions in the case of a BEC. Due to this resemblance, the term atom laser has been coined for propagating beams of atoms coupled out from a BEC [47]. As an optical laser, an atom laser needs a trapped and macroscopically occupied lasing mode - the BEC - and some mechanism to couple the lasing mode to an untrapped mode. For BECs confined in magnetic traps, this is done by coupling the atoms to a magnetically untrapped state. Atoms in the untrapped state leave the trapping region under the influence of gravity and the mean-field potential of the still trapped atoms. Raman output coupling can give the atoms an additional momentum kick away from the trapping region.

We now turn our focus to experimental techniques to couple atoms from a magnetically trapped BEC to an untrapped state by changing the internal state of the atoms.

Output coupling without momentum transfer The first output couplers have been realized with RF pulses driving magnetic dipole transitions between the magnetically trapped and untrapped $m_F = 0$ Zeeman states within the same hyperfine state. The first demonstration of an atomlaser [37] used short RF pulses to output couple from a BEC of sodium atoms. A quasi-continuous long pulse RF output coupler was demonstrated in 1999 [6]. RF output coupling mutually couples all the (in first order) equally spaced magnetic substates, i.e. an atom in the untrapped state can be coupled to the anti-trapped state.

Two-state coupling without momentum transfer, i.e coupling between magnetically trapped and untrapped states of different hyperfine states, can be realized by a single-photon microwave (MW) transition [39, 47]. Here, the adressed states are closer to a two-level system, since they have an energy difference in the order of the hyperfine splitting ($\Delta E_{\mathrm{hfs}}/\mathrm{h} \sim 6.83$ GHz in ^{87}Rb), while the energy difference of magnetic substates is given by the linear Zeeman shift which is orders of magnitudes smaller ($\Delta E/\mathrm{h} \sim 1$ MHz for small fields in ^{87}Rb).

Output coupling with momentum transfer: Raman output coupling The coupling between a trapped and an untrapped state can also be realized with a two-photon Raman transition. Two-photon Raman processes involve three atomic energy levels, the trapped

state, the untrapped state and a virtual state close to an excited atomic eigenstate. Two laser fields with a frequency difference $\Delta\omega = \omega_1 - \omega_2$ matching the energy splitting of the desired transition $\Delta E = \hbar\,(\omega_1 - \omega_2)$ couple the trapped and untrapped state via the virtual state. The atoms absorb a photon with frequency ω_1 and are stimulated to emit one with frequency ω_2. With each two-photon transition, momentum equal to $\hbar(\mathbf{k_1} - \mathbf{k_2})$ is imparted onto the atom, where $\mathbf{k_i}$ is the wave vector of the laser field. In contrast to RF output coupling, where one low-energy photon is exchanged, Raman transitions can give a significant momentum kick to the atoms as they leave the trap. The first Raman output coupler was demonstrated in 1999 [27].

In this thesis we document the setup of a Raman laser system (chapter 5) to be implemented into the Rb2 setup. It is designed to couple magnetically trapped and untrapped states of different hyperfine levels in the ^{87}Rb groundstate ($|F = 1, m_F = -1\rangle \leftrightarrow |F = 2, m_F = 0\rangle$). Further, we show the results obtained by RF- and MW output coupling from a BEC confined in a doublewell potential (chapter 4).

Structure of this thesis

This thesis is organized as follows:

- chapter 2 gives a theoretical description of the Atom-Light interaction in two- and three-level atoms, including two-photon Raman transitions.
- chapter 3 describes the main components of the Rb2 experiment and provides the experimental context for the work carried out for this thesis.
- chapter 4 summarizes the results obtained for RF- and MW output coupling.
- chapter 5 gives a detailed description of the laser system designed to drive two-photon transitions both between internal and external states.
- chapter 6 provides a conclusion and an outlook and describes the next steps towards non-destructive measurements of Bose-Einstein condensates in the Rb2 experiment.

2 Atom-Light Interaction

This chapter gives a theoretical description of the interaction of an atom with light. We start by the description of a two level atom interacting with light and derive Rabi oscillations in a two level atom both for the undamped and damped case. The results will be used in chapter 4, for the analysis of the coupling of the two ^{87}Rb hyperfine levels with microwave radiation. We will then look at the interaction of a three level atom with two light fields and derive the effective coupling of two internal atomic states via a third level. This provides the theoretical basis for the Raman laser system presented in chapter 5.

2.1 Two level atom

2.1.1 Rabi oscillations

In a semiclassical approach, the atom is considered as a two level system interacting with a classical monochromatic light field.

Approximations

The interaction of atoms with light is a resonance phenomenon, meaning that if the frequency of the light is close to the frequency of a specific optical transition in the atom, the interaction will be strong. On the other hand, if the incident light is off-resonance, the atom - light interaction will be weak. Therefore atomic energy levels that are off resonance can be ignored in a good first approximation, and the atom can be described as a two level system interacting with light.

The second approximation made is the treatment of light as a classical electromagnetic wave instead of a quantized field. This is valid if a large number of photons is interacting with the atoms [21, 65], i.e if the photon number fluctuations of the electromagnetic field are small compared to the mean number of photons [41].

Time-dependent Schrödinger equation

We start by looking at the evolution of the state $|\Psi\rangle$ of the system, which follows the time-dependent Schrödinger equation:

$$\hat{H}\,|\Psi(t)\rangle = \mathrm{i}\hbar\frac{\partial\,|\Psi(t)\rangle}{\partial t} \tag{2.1}$$

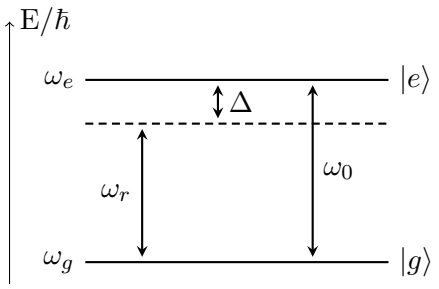

FIGURE 2.1: Energy level diagram for a two level atom with ground state $|g\rangle$ and excited state $|e\rangle$ and corresponding energies $\hbar\omega_g$ and $\hbar\omega_e$. ω_r denotes the angular frequency of the electromagnetic radiation and ω_0 the resonance frequency of the transition $|g\rangle \leftrightarrow |e\rangle$. Δ is the detuning from resonance $\omega_0 - \omega_r$.

We can split the Hamiltonian $\hat{H}$ in two parts: $\hat{H} = \hat{H}_0 + \hat{H}_{\text{int}}(t)$. The time-dependent part $\hat{H}_{\text{int}}(t)$ accounts for an external perturbation of the atom, in our case for the interaction of the atom with light.

Description of the two level atom The time-independent part $\hat{H}_0$ describes the unperturbed atom, whose eigenstates are a groundstate $|g\rangle$ and an excited state $|e\rangle$. The unperturbed Hamiltonian expressed in its eigenbasis is then given by $\hat{H}_0 = \hbar(\omega_e |e\rangle \langle e| + \omega_g |g\rangle \langle g|)$ and has the following solutions:

$$\begin{aligned} \hat{H}_0 |e\rangle &= \hbar\omega_e |e\rangle \\ \hat{H}_0 |g\rangle &= \hbar\omega_g |g\rangle \end{aligned} \tag{2.2}$$

where $\hbar\omega_g$ is the groundstate energy and $\hbar\omega_e$ the energy of the excited atomic state. We can define the resonance frequency ω_0 in terms of the two eigenenergies:

$$\omega_0 = \omega_e - \omega_g \tag{2.3}$$

The internal state $|\Psi\rangle$ of the two level atom is expressed as a superposition of an excited state $|e\rangle$ and a groundstate $|g\rangle$:

$$|\Psi(t)\rangle = b_e(t) |e\rangle + b_g(t) |g\rangle \tag{2.4}$$

Normalization requires that the coefficients $b_e(t)$ and $b_g(t)$ satisfy
$|b_e(t)|^2 + |b_g(t)|^2 = 1$.

Description of the light field Now we consider the electromagnetic field interacting with the atom. We assume it is monochromatic with angular frequency ω_r:

$$\mathbf{E}(t) = \epsilon E_0 \cos(\omega_r t) = \epsilon \frac{E_0}{2} \left(\mathrm{e}^{-\mathrm{i}\omega_r t} + \mathrm{e}^{\mathrm{i}\omega_r t} \right) \tag{2.5}$$

where E_0 denotes the maximum amplitude vector of the electric field and ϵ its polarization. The spatial dependence of the field is ignored, we only describe the field at the position of the atom. This is valid if we assume that the field is uniform over the extent of the atom and especially holds for optical transitions, where the wavelength λ of the field is in the order of hundreds of nm, much larger than the size of the atom a_0 in the order of Å. [20, 38, 55]

Electric dipole approximation The interacting part of the Hamiltonian within the electric dipole approximation is given by [16, 20, 65]

$$\hat{H}_{\text{int}} = -\mathbf{d} \cdot \mathbf{E} \tag{2.6}$$

where $\mathbf{d}$ is the atomic dipole operator in terms of the atomic electron position, $\mathbf{d} = -\mathrm{e} \cdot \hat{\mathbf{r}}$, if we assume that the interaction is dominated by the interaction with a single electron. Using the completness relation $|e\rangle \langle e| + |g\rangle \langle g| = \mathbb{1}$ the dipole operator in terms of the atomic eigenstates $|g\rangle$ and $|e\rangle$ is

$$\mathbf{d} = \langle g| \mathbf{d} |e\rangle |g\rangle \langle e| + \langle e| \mathbf{d} |g\rangle |e\rangle \langle g| \tag{2.7}$$

The diagonal matrix elements of the dipole operator are zero since $\langle g| \hat{\mathbf{r}} |g\rangle = \langle e| \hat{\mathbf{r}} |e\rangle = 0$, the odd position operator $\hat{\mathbf{r}}$ only couples between states with different parity, i.e $|g\rangle$ and $|e\rangle$.

We define the coupling strength Ω_R proportional to the off-diagonal dipole matrix elements such that

$$\hbar\Omega_R = - \langle g| \mathbf{d} |e\rangle \epsilon E_0 \tag{2.8}$$

Using these definitions the interaction Hamiltonian defined in Equation 2.6 can be written as

$$\hat{H}_{\text{int}} = (\hbar\Omega_R |g\rangle \langle e| + \hbar\Omega_R^* |e\rangle \langle g|) \cdot \cos(\omega_r t) \tag{2.9}$$

Equations of motion Inserting $\hat{H}_0$ and $\hat{H}_{\text{int}}$ and the ansatz in Equation 2.4 into the Schrödinger equation (Equation 2.1) and projection onto the eigenstates yields the equations of motion for the coefficients b_e and b_g:

$$\begin{aligned} \mathrm{i}\dot{b}_e(t) &= \omega_e b_e(t) + \Omega_R^* b_g(t) \\ \mathrm{i}\dot{b}_g(t) &= \omega_g b_g(t) + \Omega_R b_e(t) \end{aligned} \tag{2.10}$$

To further simplify this expression, the variables $b_i(t)$ are transformed into $c_i(t) = b_i \mathrm{e}^{\mathrm{i}\omega_i t}$: a suitable phase for the variables $b_i(t)$ is chosen. This will only shift the zero-point energy and is algebraically equivalent to a transformation to a rotating frame [36, 53]. Using the resonance frequency ω_0 defined in Equation 2.3 and decomposing $\cos(\omega_r t) = \frac{1}{2}\left(\mathrm{e}^{-\mathrm{i}\omega_r t} + \mathrm{e}^{\mathrm{i}\omega_r t}\right)$, the equations of motion become

$$\begin{aligned} \dot{c}_e(t) &= -\frac{\mathrm{i}}{2}\Omega_R^* c_g(t)(\mathrm{e}^{\mathrm{i}(\omega_0+\omega_r)t} + \mathrm{e}^{-\mathrm{i}(-\omega_0+\omega_r)t}) \\ \dot{c}_g(t) &= -\frac{\mathrm{i}}{2}\Omega_R c_e(t)(\mathrm{e}^{\mathrm{i}(-\omega_0+\omega_r)t} + \mathrm{e}^{-\mathrm{i}(\omega_0+\omega_r)t}) \end{aligned} \tag{2.11}$$

We introduce the detuning Δ of the laser frequency ω_r from the resonance frequency ω_0: $\Delta \equiv \omega_0 - \omega_r$.

Rotating wave approximation (RWA) In the case of small detunings compared to the transition frequency, i.e $\Delta = \omega_0 - \omega_r \ll \omega_r + \omega_0$, the fast oscillating terms containing $\omega_r + \omega_0$ can be neglected. They will average to zero when looking at a timescale associated with $\omega_0 - \omega_r$ [16].

In our case, for ^{87}Rb the energy splitting between ground state and first excited state corresponds to $\omega_0/2\pi = 384$ THz [54] whereas lasers are detuned up to $\Delta/2\pi = 100$ GHz, so this approach is justified.

Now those two coupled differential equations take a form that can easily be solved:

$$\dot{c}_e(t) = -\mathrm{i}\frac{\Omega_R^*}{2} c_g(t)\mathrm{e}^{-\mathrm{i}\Delta t} \tag{2.12a}$$

$$\dot{c}_g(t) = -\mathrm{i}\frac{\Omega_R}{2} c_e(t)\mathrm{e}^{\mathrm{i}\Delta t} \tag{2.12b}$$

Differentiating Equation 2.12a and inserting Equation 2.12b yields

$$\ddot{c}_e(t) + \mathrm{i}\Delta\dot{c}_e(t) + \frac{{\Omega_R}^2}{4} c_e(t) = 0 \tag{2.13}$$

Rabi Oscillations We define the effective Rabi frequency Ω_{eff} as

$$\Omega_{\text{eff}} = \sqrt{\Delta^2 + {\Omega_R}^2} \tag{2.14}$$

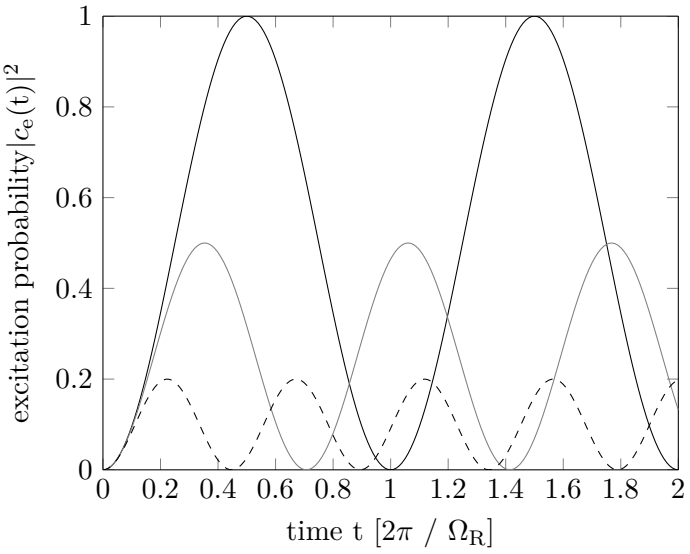

FIGURE 2.2: Population of the excited state as described by Equation 2.16 for different detunings Δ. At resonance ($\Delta = 0$, black line); $\Delta = \Omega_R$ (grey line); $\Delta = 2\Omega_R$ (black dashed line).

Using the initial condition, that all the atoms are in the lower energy state $|g\rangle$, i.e. $c_g(t = 0) = 1$ and $c_e(t = 0) = 0$, we get the following solutions for $c_e(t)$ and $c_g(t)$:

$$c_g(t) = \mathrm{e}^{\mathrm{i}\Delta t/2}\left[\cos\left(\frac{\Omega_{\text{eff}}}{2}t\right) - \mathrm{i}\frac{\Delta}{\Omega_{\text{eff}}}\sin\left(\frac{\Omega_{\text{eff}}}{2}t\right)\right] \tag{2.15a}$$

$$c_e(t) = -\mathrm{i}\mathrm{e}^{-\mathrm{i}\Delta t/2}\frac{\Omega_R}{\Omega_{\text{eff}}}\sin\left(\frac{\Omega_{\text{eff}}}{2}t\right) \tag{2.15b}$$

This means that the atomic state oscillates between $|e\rangle$ and $|g\rangle$. This behavior is called Rabi oscillation or Rabi flopping [21]. The probability of being in $|e\rangle$ is given by

$$|c_e(t)|^2 = \left(\frac{\Omega_R}{\Omega_{\text{eff}}}\right)^2 \cdot \sin^2\left(\frac{\Omega_{\text{eff}}}{2}t\right) \tag{2.16}$$

When detuning the light field from the atomic resonance ω_0, the frequency Ω_{eff} of this oscillation increases (see Equation 2.14) while the amplitude $\Omega_R/\Omega_{\text{eff}}$ decreases. In order to achieve a full population transfer of an ensemble of atoms, the light field needs to be resonant with the atomic transition. Figure 2.2 shows this behaviour for different detunings Δ.

2.1.2 Damped Rabi oscillations

Density operators In order to take losses of coherence and spontaneous population decay into account, the two level system is best described with the density matrix formalism. We will just briefly introduce the basics needed for the description of damped Rabi oscillations

in a two level system with density matrices. A detailed introduction can be found in textbooks such as reference [50]. The density matrix ρ is defined as

$$\rho = \sum_i p_i \left|\Psi_i\right\rangle \left\langle\Psi_i\right| \tag{2.17}$$

where p_i describes the (classical) probability of the system being in one of the states $|\Psi_i\rangle$. The probabilities are normalized ($\sum p_i = 1$) and the expectation value for any observable $\hat{A}$ is expressed by the trace: $\langle\hat{A}\rangle = \mathrm{tr}(\rho\hat{A})$. The density operator ρ also describes mixed states and can account for incoherent processes.

Reformulating the problem above in this formalism gives the density operator for the system, using the state defined in Equation 2.4 with the matrix representation in the basis $\{|e\rangle, |g\rangle\}$:

$$\rho = \left|\Psi_i\right\rangle \left\langle\Psi_i\right| = \begin{pmatrix} \rho_{ee} & \rho_{eg} \\ \rho_{ge} & \rho_{gg} \end{pmatrix} = \begin{pmatrix} |c_e|^2 & c_e c_g^* \\ c_g c_e^* & |c_g|^2 \end{pmatrix} \tag{2.18}$$

Equations of motion Since the time-derivatives of $c_e(t)$ and $c_g(t)$ have already been calculated above, Equation 2.11 can directly be used to find the equations of motion for the density matrix elements:

$$\begin{aligned} \dot{\rho}_{ee} &= \partial_t(c_e \cdot c_e^*) = \frac{\mathrm{i}\Omega_R}{2}\left(\rho'_{eg} - \rho'_{ge}\right) \\ \dot{\rho}_{gg} &= -\dot{\rho}_{ee} = -\frac{\mathrm{i}\Omega_R}{2}\left(\rho'_{eg} - \rho'_{ge}\right) \\ \dot{\rho}'_{ge} &= \partial_t(c_g \cdot c_e^*) = -\mathrm{i}\Delta\rho'_{ge} - \frac{\mathrm{i}\Omega_R}{2}\left(\rho_{ee} - \rho_{gg}\right) \\ \dot{\rho}'_{eg} &= \partial_t\rho'^*_{ge} = \mathrm{i}\Delta\rho'_{ge} + \frac{\mathrm{i}\Omega_R}{2}\left(\rho_{ee} - \rho_{gg}\right) \end{aligned} \tag{2.19}$$

where $\rho'_{ge} = \rho_{ge}\mathrm{e}^{-\mathrm{i}\Delta t}$. We further used the normalization condition $\rho_{ee} + \rho_{gg} = 1$ $\Rightarrow \dot{\rho_{ee}} = -\dot{\rho_{gg}}$ and $\rho'_{ge} = \rho'^*_{eg}$. Note that the density operator is a hermitian operator, i.e $\rho_{ge} = \rho^*_{eg}$.

Population decay and decoherence We now add decay terms to model spontaneous emission and loss of coherence due to collisions. With $\Omega_R = \Delta = 0$ the terms have the form [55]

$$\begin{aligned} \dot{\rho}_{ee} &= -\Gamma\rho_{ee} \\ \dot{\rho}_{gg} &= +\Gamma\rho_{ee} \\ \dot{\rho}'_{ge} &= -\left(\frac{\Gamma}{2} + \gamma_c\right)\rho'_{ge} \\ \dot{\rho}'_{eg} &= -\left(\frac{\Gamma}{2} + \gamma_c\right)\rho'_{eg} \end{aligned} \tag{2.20}$$

The excited state population ρ_{ee} decays at a rate Γ and the population in the ground state grows at the same rate. These terms account for spontaneous emission from the excited state to the ground state. $\Gamma = \tau^{-1}$, where τ is the lifetime of the excited state. The off-diagonal terms or coherences $\rho'_{ge} = \rho'^{*}_{eg}$ damp at a rate $\gamma = \Gamma/2 + \gamma_c$ where the term $\Gamma/2$ is needed for consistency with the spontaneous emission. The additional damping term γ_c models decay beyond spontaneous emission. It models dephasing mechanisms, that do not change the state populations, such as collisions between the atoms. [55].

Optical Bloch equations We combine these damping terms (Equation 2.20) with the terms describing the time evolution due to the Hamiltonian (Equation 2.19) to get the optical Bloch equations:

$$\begin{aligned}
\dot{\rho}_{ee} &= \frac{\mathrm{i}\Omega_R}{2}\left(\rho'_{eg} - \rho'_{ge}\right) - \Gamma\rho_{ee} \\
\dot{\rho}_{gg} &= -\frac{\mathrm{i}\Omega_R}{2}\left(\rho'_{eg} - \rho'_{ge}\right) + \Gamma\rho_{ee} \\
\dot{\rho}'_{ge} &= -\left(\gamma + \mathrm{i}\Delta\right)\rho'_{ge} - \frac{\mathrm{i}\Omega_R}{2}\left(\rho_{ee} - \rho_{gg}\right) \\
\dot{\rho}'_{eg} &= -\left(\gamma - \mathrm{i}\Delta\right) + \frac{\mathrm{i}\Omega_R}{2}\left(\rho_{ee} - \rho_{gg}\right)
\end{aligned} \tag{2.21}$$

A solution A general solution for the excited state population can be found for the case of resonant light ($\Delta = 0$) and setting $\gamma_c = 0$, i.e $\gamma = \Gamma/2$. With the initial conditions $\rho_{gg}(t=0) = 1$ and $\rho_{ge}(0) = \rho_{eg}(0) = \rho_{ee} = 0$ the solution for the evolution of the excited state population ρ_{ee} is [21, 35]

$$\rho_{ee} = |c_e(t)|^2 = \frac{1}{2(1+\xi^2)}\left\{1 - \left[\cos\left(\Omega' t\right) + \frac{3\xi}{\sqrt{4-\xi^2}}\sin(\Omega' t)\right]\mathrm{e}^{-\frac{3\gamma t}{2}}\right\} \tag{2.22}$$

where $\xi = \gamma/\Omega_R$ is the ratio of damping to coupling and $\Omega' = \Omega_R \cdot \sqrt{1-\gamma/4}$ the effective coupling. Figure 2.3 shows the oscillations between $|g\rangle$ and $|e\rangle$ for different damping factors γ. Again, in order to achieve a full population transfer in an ensemble of atoms the ratio of damping factor to coupling strength ξ needs to be small.

2.1.3 Photon scattering rate

As discussed above, the optical Bloch equations (Equation 2.21) describe the excitation of a two level atom by radiation close to a transition that decays by spontaneous emission. We can find steady state solutions ($\dot{\rho} = 0$) to the equations to describe the excited state population for times much larger than the lifetime of the exited state, for $t \gg \Gamma^{-1}$. Here, we assume that no collisions occur, i.e $\gamma_c = 0$ [35, 54]:

$$\rho_{ee} = \frac{(\Omega_R/\Gamma)^2}{1 + 4(\Delta/\Gamma)^2 + 2(\Omega_R/\Gamma)^2} \tag{2.23}$$

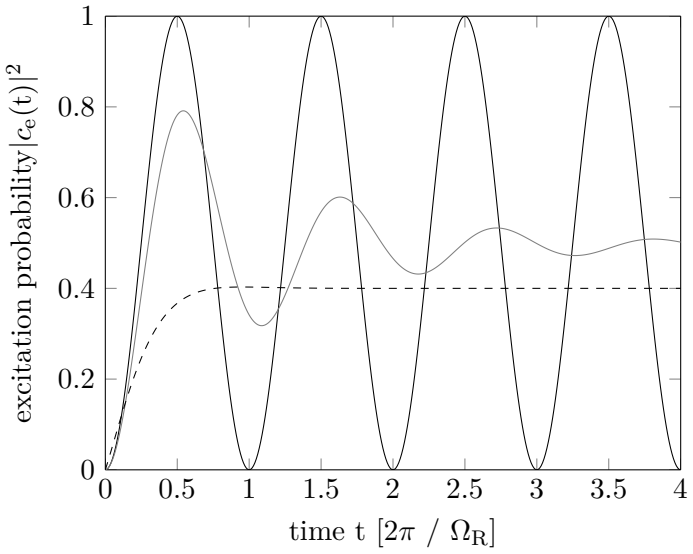

FIGURE 2.3: Population of the excited state as described by Equation 2.22 for different ξ. Black line: $\xi = 0$, grey line: $\xi = 0.1$, black dashed line: $\xi = 1$.

The total photon scattering rate R_{sc} is proportional to the excited state population and the decay rate of the excited state Γ:

$$R_{\mathrm{sc}} = \Gamma \rho_{ee} = \frac{\Gamma}{2} \frac{I/I_{\mathrm{sat}}}{1 + 4(\Delta/\Gamma)^2 + I/I_{\mathrm{sat}}} \tag{2.24}$$

Where the saturation intensity I_{sat} is defined such that [54]

$$\frac{I}{I_{\mathrm{sat}}} = 2 \left(\frac{\Omega_R}{\Gamma} \right)^2 \tag{2.25}$$

2.2 Three level atom and Raman transitions

The goal of this thesis was to construct a laser system that can drive transitions between the two hyperfine levels $|F = 1\rangle \leftrightarrow |F = 2\rangle$ in the ^{87}Rb ground state. For this we choose Raman transitions, which are two-photon processes that couple the two states, subsequently denoted as $|0\rangle$ and $|1\rangle$ via a far detuned, virtual state $|e\rangle$. Such two-photon processes can be used when the transition $|0\rangle \leftrightarrow |1\rangle$ is electric dipole-forbidden, such as transitions between different hyperfine states, or has an inconvenient frequency.[28]

We will see in chapter 5 that much stronger coupling between the two hyperfine levels of the ^{87}Rb ground state can be achieved with a Raman transition than with a single photon transition in the microwave-regime for the powers we have available in our setup.

Interaction with two light fields In order to derive this coupling strength the model of a three level atom interacting with two light fields is used. Figure 2.4 shows the energy level

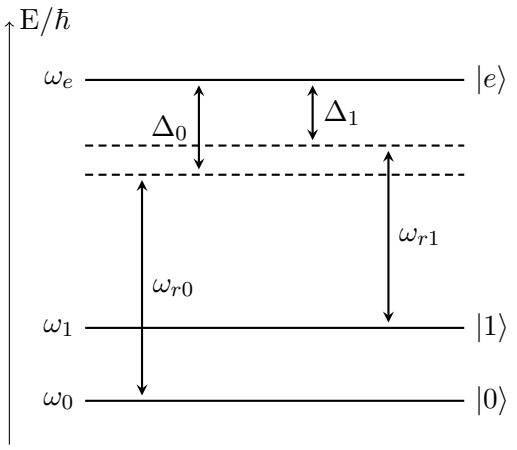

FIGURE 2.4: Energy level diagram for a three level atom interacting with two radiation fields of angular frequency ω_{r0} and ω_{r1}

diagram for such a model in a Λ-type configuration, where the energy of the intermediate level is higher than the one of the target states.

Hamiltonian of the system The problem is treated similarly as the one presented in section 2.1 and reference [28]. An atom with energy levels $|0\rangle$, $|1\rangle$ and $|e\rangle$ is perturbed by two light fields with angular frequency ω_{r0} and ω_{r1}. Further it is assumed that $\omega_{r0}, \omega_{r1} \gg \omega_1 - \omega_0$, which means that each of the light fields cannot directly couple levels $|0\rangle$ and $|1\rangle$.

The Hamiltonian of the system is given by $\hat{H} = \hat{H}_0 + \hat{H}^0_{\text{int}} + \hat{H}^1_{\text{int}}$, where the parts describing the interaction $\hat{H}_{\text{int}}$ have the same form as in section 2.1:

$$\begin{aligned}\hat{H} &= H_0 + \hat{H}^0_{\text{int}} + \hat{H}^1_{\text{int}} = \\ &= E_0 |0\rangle \langle 0| + E_1 |1\rangle \langle 1| + E_e + |e\rangle \langle e| \\ &+ \hbar \cos \omega_{r0} t (\Omega_0 |e\rangle \langle 0| + \Omega_0^* |0\rangle \langle e|) \\ &+ \hbar \cos \omega_{r1} t (\Omega_1 |e\rangle \langle 1| + \Omega_1^* |1\rangle \langle e|)\end{aligned} \tag{2.26}$$

where Ω_i is the coupling between $|i\rangle$ and $|e\rangle$ given by $\hbar\Omega_i = E_i d_{ei}$, E_i being the amplitude of the electromagnetic field and d_{ei} the dipole moment for the transition between $|i\rangle$ and $|e\rangle$.

Equations of motion and RWA Using the ansatz $|\Psi(t)\rangle = b_0(t)|0\rangle + b_1(t)|1\rangle + b_e(t)|e\rangle$ for the Schrödinger equation with the Hamiltonian in Equation 2.26 yields the equations

of motion:

$$\begin{aligned} \mathrm{i}\dot{b}_0 &= \omega_0 b_0 + \cos(\omega_{r0}t)\Omega_0^* b_e \\ \mathrm{i}\dot{b}_1 &= \omega_1 b_1 + \cos(\omega_{r1}t)\Omega_1^* b_e \\ \mathrm{i}\dot{b}_e &= \omega_e b_e + \cos(\omega_{r0}t)\Omega_0 b_0 + \cos(\omega_{r1}t)\Omega_1 b_1 \end{aligned} \tag{2.27}$$

We introduce the detunings of the light fields with ω_{r0} and ω_{r1} from the atomic transitions as follows: The detunings between the two lasers and the atomic transitions are $\Delta_0 = \omega_e - \omega_0 - \omega_{r0}$ and $\Delta_1 = \omega_e - \omega_1 - \omega_{r1}$. The average detuning is given by $\Delta = \frac{\Delta_0 + \Delta_1}{2}$ and the two photon detuning by $\delta = \Delta_0 - \Delta_1$.

We choose a frame rotating at $\mathrm{e}^{-\mathrm{i}\hat{H}'t/\hbar}$ with $\hat{H}'$ given by

$$\hat{H}' = \hbar \begin{pmatrix} \omega_0 + \frac{\delta}{2} & 0 & 0 \\ 0 & \omega_1 - \frac{\delta}{2} & 0 \\ 0 & 0 & \omega_e - \Delta \end{pmatrix} \tag{2.28}$$

Using the detunings defined above and applying the RWA (i.e dropping the terms that oscillate at $2\omega_{ri}$), the equations of motion become

$$\begin{pmatrix} \dot{c}_0(t) \\ \dot{c}_1(t) \\ \dot{c}_e(t) \end{pmatrix} = -\frac{\mathrm{i}}{2} \begin{pmatrix} -\delta & 0 & \Omega_0 \\ 0 & \delta & \Omega_1 \\ \Omega_0^* & \Omega_1^* & 2\Delta \end{pmatrix} \begin{pmatrix} c_0(t) \\ c_1(t) \\ c_e(t) \end{pmatrix} \tag{2.29}$$

where the state amplitudes $b_i(t)$ have also been transformed to the rotating frame, i.e $c_i = b_i(t)\mathrm{e}^{\mathrm{i}\hat{H}'t/\hbar}$.

Adiabatic elimination Now it is assumed that the excited state $|e\rangle$ is initially not populated and since the light fields are far detuned by Δ, such that $\Delta \gg \Omega_0, \Omega_1$, the change in the population of $|e\rangle$ can be neglected, i.e $\dot{c}_e = 0$. This step is known as adiabatic elimination. [28]

Therefore,

$$2\mathrm{i}\dot{c}_e(t) = \Omega_0^* c_0(t) + \Omega_1^* c_1(t) + 2\Delta c_e(t) = 0 \tag{2.30}$$

or

$$c_e(t) = -\frac{\Omega_0^* c_0(t) + \Omega_1^* c_1(t)}{2\Delta} \tag{2.31}$$

which can be substituted into Equation 2.29, yielding the reduced equations of motion for the evolution of $c_0(t)$ and $c_1(t)$:

$$\begin{pmatrix}\dot{c}_0(t)\\ \dot{c}_1(t)\end{pmatrix} = \frac{\mathrm{i}}{2}\begin{pmatrix}\delta + \frac{|\Omega_0|^2}{2\Delta} & \frac{\Omega_0\Omega_1^*}{2\Delta}\\ \frac{\Omega_0^*\Omega_1}{2\Delta} & -\delta + \frac{|\Omega_1|^2}{2\Delta}\end{pmatrix}\begin{pmatrix}c_0(t)\\ c_1(t)\end{pmatrix} \tag{2.32}$$

The zero point energy is shifted by subtracting $\frac{|\Omega_0|+|\Omega_1|}{4\Delta}$ from the diagonal terms:

$$\begin{pmatrix}\dot{c}_0(t)\\ \dot{c}_1(t)\end{pmatrix} = -\frac{\mathrm{i}}{2}\begin{pmatrix}-\delta_e & \Omega_e\\ \Omega_e^* & \delta_e\end{pmatrix}\begin{pmatrix}c_0(t)\\ c_1(t)\end{pmatrix} \tag{2.33}$$

where the effective detuning is given by $\delta_e = \delta - \frac{|\Omega_1|^2-|\Omega_0|^2}{4\Delta}$ and the coupling strength for the effective two level system consisting of levels $|0\rangle$ and $|1\rangle$, the two photon Rabi frequency is given by:

$$\Omega_e = -\frac{\Omega_0\Omega_1^*}{2\Delta} \tag{2.34}$$

The three level atom oscillates between the ground states at an effective frequency $\tilde{\Omega}_e = \sqrt{\Omega_e^2 + \delta_e^2}$ and an amplitude given by $\Omega_e^2/\tilde{\Omega}_e^2$. [16] This means, that a full population transfer in an ensemble of atoms can be achieved even if the individual detunings Δ_0 are Δ_1 are large, as long as the effective detuning δ_e is zero.

We have seen in Equation 2.24 that the single photon scattering rate is proportional to Δ^{-2} whereas the coupling between two groundstates of a three level atom is $\Omega_e \sim \Delta^{-1}$ as just derived. By using far detuned laser fields, one can therefore suppress scattering to the excited state and still achieve high two-photon Rabi frequencies. This will be the main argument to operate the laser for the Raman system detuned by $\Delta/2\pi$ =100 GHz from the ^{87}Rb D2 - line.

Reference [28] derives solutions for the three level system described on the last pages without using adiabatic elimination to remove the excited state. The population in the excited state will undergo oscillations at a higher frequency and a much smaller amplitude than the oscillations of the populations in the groundstates. The amplitude and frequency of $|c_e(t)|^2$ depends mainly on the ratio of the Rabi frequencies Ω_0, Ω_1 to the average detuning Δ. It is shown that for $\Omega_0/\Delta = \Omega_1/\Delta = 10^{-1}$ and for $\delta = 0$ the amplitude of $|c_e(t)|^2$ is about 5% of the amplitude of $|c_0(t)|^2$ or $|c_1(t)|^2$. With the parameters we choose for the Raman system $\Omega_0/\Delta \sim /\Omega_1/\Delta \sim 10^{-3}$ we can assume that the adiabatic elimination is a valid approximation to describe our system.

2.3 Dressed state picture

In the dressed state picture, the state of the light field and internal atomic state are described together. The coupling of an atom to the light field gives rise to new eigenstates,

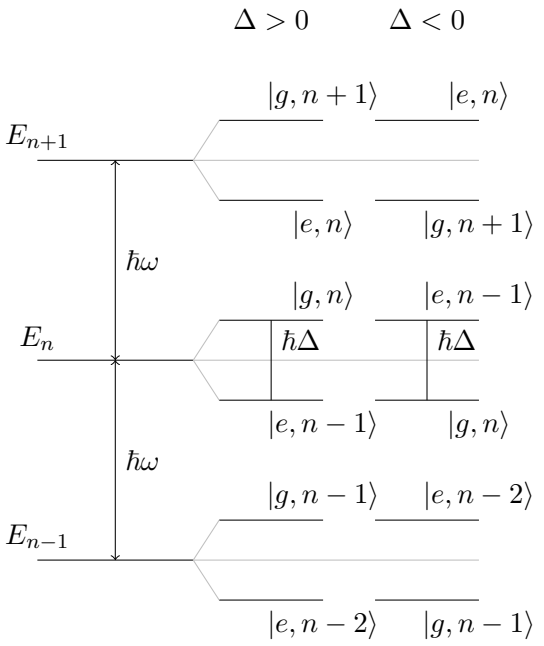

FIGURE 2.5: Manifolds of uncoupled eigenstates of $\hat{H}_0+\hat{H}_L$. The energy spacing between the manifolds is ω_L, the spacing between the eigenstates is $\hbar\Delta$. Depending on the sign of the detuning states connected to $|g\rangle$ or $|e\rangle$ have a larger energy. Left: $\Delta > 0$, right: $\Delta < 0$. For zero detuning, the states $|g, n\rangle$ and $|e, n-1\rangle$ are degenerate.

the *dressed states* [41]. As in the beginning of this chapter, we use the model of a two level atom with eigenstates $|g\rangle$ and $|e\rangle$ with resonance frequency ω_0 and internal Hamiltonian $\hat{H}_0$ (Equation 2.2).

Hamiltonian of the laser field The laser field is treated as a quantized field with creation and annihilation operators $\hat{a}^\dagger$ and $\hat{a}$ for photons in the laser mode. The Hamiltonian of the laser field with frequency ω_L is

$$\hat{H}_L = \left(\hat{a}^\dagger\hat{a} + \frac{1}{2}\right)\hbar\omega_L \tag{2.35}$$

The eigenstates of the light field are the photon number states $|n\rangle$, eigenstates of $\hat{n} = \hat{a}^\dagger\hat{a}$, such that $\hat{n}\,|n\rangle = n\,|n\rangle$. As above, we assume that the laser intensity is high, i.e the number fluctuations are small compared to the mean photon number, $\Delta n \ll \langle n\rangle$.

The uncoupled states of the atomic field and laser field, the eigenstates of the Hamiltonian $\hat{H}_0 + \hat{H}_L$ are denoted as $|g, n\rangle$ and $|e, n\rangle$ $(= |e\rangle \otimes |n\rangle$, 'atom in $|e\rangle$ and n photons in the laser mode') with eigenenergies $E_{g,n} = (n+1/2)\hbar\omega_L$ and $E_{g,n} = (n+1/2)\hbar\omega_L + \hbar\omega_0$. Here we choose the zero point energy such that $\hbar\omega_g = 0$. For small detunings $\Delta = \omega_L - \omega_0$, $|\Delta| \ll \omega_0, \omega_L$ these unperturbed eigenstates can be grouped in manifolds M_n of two eigenstates $|g, n\rangle$ and $|e, n-1\rangle$ separated by the detuning $\hbar\Delta$ around E_n. This is sketched in Figure 2.5.

Coupling We now add the interaction Hamiltonian in the RWA to the picture, i.e we neglect the terms $\hat{a}\,|g\rangle\,\langle e|$ and $\hat{a}^\dagger\,|e\rangle\,\langle g|$.

$$\hat{H}_{\text{int}} = \frac{\hbar\Omega_0}{2}\left(\hat{a}\,|e\rangle\,\langle g| + \hat{a}^\dagger\,|g\rangle\,\langle e|\right) \tag{2.36}$$

Here Ω_0 denotes the coupling strength for one photon between $|g,1\rangle$ and $|e,0\rangle$. The dipole matrix element between $|g,n\rangle$ and $|e,n-1\rangle$ is

$$\langle g,n|\,\hat{H}_{\text{int}}\,|e,n-1\rangle = \langle e,n-1|\,\hat{H}_{\text{int}}\,|g,n\rangle = \frac{\hbar\Omega_0}{2}\sqrt{n} \simeq \frac{\hbar\Omega_R}{2} \tag{2.37}$$

where the mean Rabi frequency is $\Omega_R = \sqrt{\langle n\rangle}\Omega_0$. We can use this if we assume that the light field is populated with a large amount of photons such that $\langle n\rangle \gg \Delta n$ and the matrix elements in the manifolds M_{n+1} and M_n are almost the same. For a manifold M_n the Hamiltonian then is:

$$\hat{H}_n = E_n + \frac{\hbar}{2}\begin{pmatrix} -\Delta & \Omega_R \\ \Omega_R & \Delta \end{pmatrix} \tag{2.38}$$

Dressed states Its eigenenergies are

$$E_\pm = E_n \pm \frac{\hbar}{2}\sqrt{\Delta^2 + \Omega_R^2} = E_n \pm \frac{\hbar}{2}\tilde{\Omega} \tag{2.39}$$

with generalized Rabi frequency $\tilde{\Omega} = \sqrt{\Delta^2 + \Omega_R^2}$. Its eigenstates are superpositions of the states $|g,n\rangle$ and $|e,n-1\rangle$:

$$\begin{aligned} |+,n\rangle &= \sin\frac{\theta}{2}\,|g,n\rangle + \cos\frac{\theta}{2}\,|e,n-1\rangle \\ |-,n\rangle &= -\cos\frac{\theta}{2}\,|g,n\rangle + \sin\frac{\theta}{2}\,|e,n-1\rangle \end{aligned} \tag{2.40}$$

with the dressing angle θ defined by

$$\cos\theta = -\frac{\Delta}{\tilde{\Omega}},\ \sin\theta = -\frac{\Omega_R}{\tilde{\Omega}} \tag{2.41}$$

These are the dressed states, superpositions of of the uncoupled bare states $|g,n\rangle$ and $|e,n-1\rangle$. Figure 2.6 shows the energy of the eigenstates depending on the detuning Δ with and without coupling. On resonance ($\Delta = 0$) the bare states are degenerate, while the dressed states are separated by an energy difference $\hbar\Omega_R$ and an avoided crossing is observed.

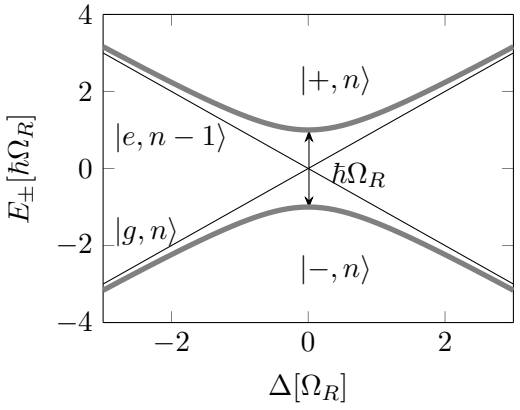

FIGURE 2.6: Eigenenergies of dressed (thick grey line) and bare states (black) depending on the detuning. At zero detuning, the dressed states have an energy difference of $\hbar\Omega_R$ and show an avoided crossing.

2.4 Momentum transfer

In this chapter we dealt with the change of an atom's internal state due to optical transitions. Due to momentum conservation, each time a photon of wavelength λ is absorbed or emitted by an atom of mass m, the atomic velocity changes by the recoil velocity $\mathbf{v}_{\text{rec}}$ given by

$$\mathbf{v}_{\text{rec}} = \frac{\hbar\mathbf{k}}{m} \tag{2.42}$$

where $\mathbf{k}$ is the light's wave vector with $|\mathbf{k}| = 2\pi/\lambda$.

Two-level atom The interaction of light therefore not only couples the atom's internal states $|g\rangle \leftrightarrow |e\rangle$, but also its momentum states $|\mathbf{p}\rangle \leftrightarrow |\mathbf{p} \pm \hbar\mathbf{k}\rangle$. For the dipole interaction considered above, the ground state in a given momentum state $|g, \mathbf{p}\rangle$ couples to a single momentum state in the excited state $|e, \mathbf{p} + \hbar\mathbf{k}\rangle$.[16]

In coupling to a different momentum state, we have to take the change in the atom's kinetic energy into account, which will shift the resonance frequency ω_0. The detuning $\Delta = \omega_0 - \omega_r$ defined above is only an approximated detuning, valid for an atom at rest and neglecting the change in its kinetic energy due to the absorption of a photon. We modify it to take the atom's momentum into account:

$$\Delta(\mathbf{p}) = \Delta + \frac{\mathbf{p}\cdot\mathbf{k}}{m} + \omega_{\text{rec}} \tag{2.43}$$

where $\omega_{\text{rec}} = \frac{\hbar k^2}{2m}$ is the single-photon recoil frequency that accounts for the change in the atom's kinetic energy. Note that we also took the change in the resonance frequency due to the Doppler shift into account.

Raman transitions For the three-level atom interacting with two light fields, we consider coupling between the states $|0, \mathbf{p}\rangle \leftrightarrow |e, \mathbf{p} + \hbar\mathbf{k_0}\rangle \leftrightarrow |1, \mathbf{p} + \hbar\mathbf{k_e}\rangle$, where $\mathbf{k_i}$ is the wave vector of the light field with frequency ω_{ri} and $\mathbf{k_e} = \mathbf{k_0} - \mathbf{k_1}$. Here we assume that the field with ω_0 initially drives a photon absorption process and ω_1 stimulates a photon emission.[16] We redefine the detunings in the description of the three-level atom interacting with two light fields accordingly:

$$\Delta_0(\mathbf{p}) = \Delta_0 + \frac{\mathbf{p} \cdot \mathbf{k_0}}{m} + \omega_{\mathrm{rec}_0} \tag{2.44a}$$

$$\Delta_1(\mathbf{p}) = \Delta + \frac{\mathbf{p} \cdot \mathbf{k_1}}{m} + \omega_{\mathrm{rec}_1} \tag{2.44b}$$

The two-photon detuning δ is now

$$\delta(\mathbf{p}) = \delta + \frac{\mathbf{p} \cdot \mathbf{k_e}}{m} + \omega_{\mathrm{rec}_e} \tag{2.45}$$

In the case of co-propagating laser beams and the resonance frequency much smaller than the frequency of the 2 laser fields, $|\mathbf{k_0}| \simeq |\mathbf{k_1}|$ and $k_e \simeq 0$. The two groundstates are therefore coupled with almost no momentum transfer and the two-photon resonance is momentum independent as $\delta(\mathbf{p}) \simeq 0$. Such a beam configuration is useful for coupling internal states of an ensemble of atoms equally across their momentum distribution.

In any other configuration, momentum is transferred and the resonance is momentum dependent. The transferred momentum is $\mathbf{p'} \propto \mathbf{k_e}$ with absolute value given by $|\mathbf{p'}| = 2N\hbar k \sin(\theta/2)$ for N two-photon events, where θ is the angle between the wavevectors of the two light fields $\mathbf{k_0}$ and $\mathbf{k_1}$ and $|\mathbf{k_0}| \simeq |\mathbf{k_1}| = k$ [56]. This can be used to couple different momentum states, for atomic velocity selection and to probe the atoms' momentum distribution [31].

3 The Rb2 Experiment

The Rubidium II (Rb2) experiment prepares clouds of ultracold Rubidium 87 (^{87}Rb) atoms in magnetic wire traps created by an atom chip. The experiment was first built in Heidelberg in 2002 and moved to Vienna in 2007. A detailed description of the current setup can be found in the theses written in Vienna by T. Berrada [4] and R. Bücker [9] and the references therein.

In this chapter, some basic principles of magnetic trapping will be described. Then I will give an overview of the experimental sequence and the imaging systems used to create, manipulate and image ultracold clouds or Bose-Einstein condensates of ^{87}Rb atoms in this setup.

3.1 Magnetic trapping of neutral atoms

The interaction energy of an atom with a magnetic dipole moment $\boldsymbol{\mu}$ and a magnetic field $\mathbf{B}$ is given by [3]

$$V = -\boldsymbol{\mu} \cdot \mathbf{B} \tag{3.1}$$

The interaction with an external $\mathbf{B}$-field breaks degeneracy of the atomic hyperfine levels F and gives rise to $2F + 1$ magnetic quantum numbers $m_F = \{-F, ..., F\}$. For weak magnetic fields, as long as the energy shift due to the interaction with the field is smaller than the hyperfine splitting ΔE_{hfs}, the energy shift is linear in B. For ^{87}Rb the hyperfine splitting of the ground state is $\sim$ 6.83GHz and the linear Zeeman shift 0.7 MHz/G [54].

Additionally, if the angular Larmor frequency[1] $\omega_L = g_F \mu_B |\mathbf{B}|/\hbar$ is large compared to the rate of change of the field seen by the atom, the magnetic moment of the atom can adiabatically align to the magnetic field. The interaction then takes the form of a potential depending on the magnitude of the magnetic field.

$$V_{|F,mF\rangle} = m_F g_F \mu_B |\mathbf{B}(\mathbf{r})| \tag{3.2}$$

where μ_B is the Bohr magneton and g_F the Landé factor.

[1] In a semi-classical picture this can be pictured as the frequency of the precession of atomic dipole moment about the quantization axis given by the external field

Wing's theorem [63] states that it is not possible to create local field maxima in empty space, which is a direct consequence of Maxwell's equations. In order to have a confining potential, the product $g_F \cdot m_F$ has to be greater than zero to get attracted by field minima (states with $g_F \cdot m_F > 0$ are therefore named *low field-seeking* states). For ^{87}Rb $g_F \simeq -\frac{1}{2}$ for the $F = 1$ ground state and $g_F \simeq \frac{1}{2}$ for $F = 2$. Therefore only the states $|1, -1\rangle$, $|2, 1\rangle$ and $|2, 2\rangle$ can be trapped magnetically.[2]

3.1.1 Magnetic fields to trap atoms

The Rb2 experiment usually implements elongated magnetic traps: In the transverse direction of the trap (in the (x, y)-plane), the trapping potential is created by a DC current I in a single wire on the atomchip along z together with a uniform Bias field $\mathbf{B_b} = B_b \cdot \mathbf{e_x}$ perpendicular to the wire created by external Helmholtz coils. A sketch of this configuration is shown in Figure 3.1. The longitudinal confinement is created by a pair of wires perpendicular to the trapping wire on the atom chip (*H-wires*).

The transverse fields cancel at a distance d given by

$$d = \frac{\mu_0 I}{2\pi B_b} \tag{3.3}$$

and define the trap center at a line parallel to the trapping wire for the low-field seeking atoms. The field created by the wire together with the Bias field $\mathbf{B_b}$ creates a quadrupole field in the vicinity of the trap center. As the atoms are guided along the side of the wire, such a trap configuration is called a side-guide trap [19]. At the trap center, the magnetic field gradient is

$$\frac{\partial B}{\partial r}|_{r=d} = \frac{2\pi}{\mu_0}\frac{B_b^2}{I} = \frac{B_b}{d} \tag{3.4}$$

To avoid spin changing collisions to untrapped states (Majorana transitions [3]) in the region of zero magnetic field an additional uniform offset field $\mathbf{B_0} = B_0 \cdot \hat{e}_z$ (Ioffe field) is added in the longitudinal direction (along z). This completes the Ioffe-Pritchard configuration.

The harmonic trapping potential in the transverse direction is given by [4]

$$\begin{aligned} U_\perp(x, y) &= |g_F| \cdot \mu_B \cdot B_0 + \frac{1}{2} m\omega_\perp^2 (x^2 + y^2) \\ \omega_\perp &= \sqrt{\frac{|g_F| \cdot \mu_B}{m \cdot B_0}} \frac{2\pi}{\mu_0 I} \cdot B_b^2 \end{aligned} \tag{3.5}$$

[2] Remark concerning the notation: From now on, internal spin states $|F, m_F\rangle$ will simply be denoted like this.

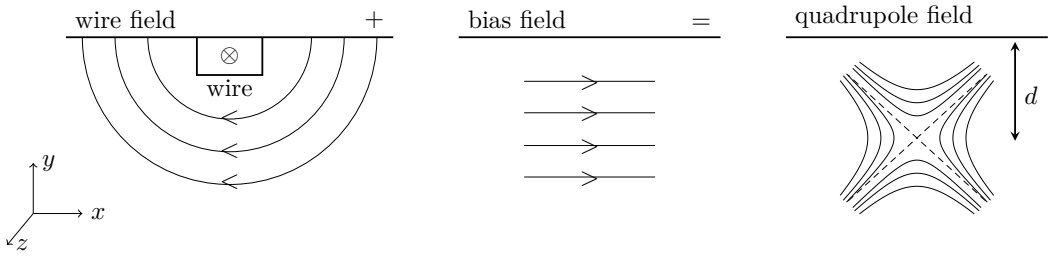

FIGURE 3.1: Sketch of the trapping fields for the transverse confinement. A circular magnetic field created by the trapping wire (left) is combined with a uniform bias field (middle).

3.1.2 Radio-frequency dressing

Radiofrequency dressing enables us to create varying trap shapes. The principle is the same as for optical dipole potentials: Coupling internal states of an atom to an external oscillating field gives rise to new eigenstates and eigenenergies, dressed sates as described in chapter 2.

As we couple magnetic substates in a static and spatially varying magnetic field $B_{\text{trap}}(\mathbf{r})$ to a magnetic RF field $B_{RF}(\mathbf{r})$ oscillating at a frequency ω, its detuning δ from the atoms' local Larmor frequency $\omega_L(\mathbf{r})$ is position dependent, and so is the coupling strength of the RF field, the Rabi frequency $\Omega_{RF} = \Omega_{RF}(\mathbf{r})$. The energy of the dressed eigenstates at the position $\mathbf{r}$ is [29, 40]

$$V_{m'}(\mathbf{r}) = m'\hbar\sqrt{\delta(\mathbf{r})^2 + \Omega_{RF}(\mathbf{r})^2} \tag{3.6}$$

with

$$\delta(\mathbf{r}) = \omega_L - \omega_{RF} = \frac{\mu_B g_F}{\hbar} B_{\text{trap}}(\mathbf{r}) \tag{3.7a}$$

$$\Omega_{RF}(\mathbf{r}) = \frac{\mu_B g_F}{2\hbar} B_{rf}(\mathbf{r}) \tag{3.7b}$$

where B_{rf} is the amplitude of the component of the RF field perpendicular to the local direction of the static trapping field [52]. The energy of the dressed states acts as potential for the atoms as long as their magnetic moment can align to the local magnetic field adiabatically. Figure 3.2 illustrates the principle of RF dressing.

RF-dressing is used to realize trapping geometries beyond harmonic potentials, such as double well trapping potentials [29, 52]. It can also be used to engineer trapping potentials for optical clocks, such that the atomic clock transition is independent of the linear Zeeman-shift, improving the precision of an atomic clock [64].

On the Rb2 experiment a Mach-Zehnder interferometer has recently been implemented with BECs confined in RF-dressed double well potentials [5]. Anharmonic trapping potentials with uneven level spacings can be created by means of RF-dressing and have been used to control motional states of BECs to create twin-atom beams [10] or to implement a Ramsey interferometer with motional states [61].

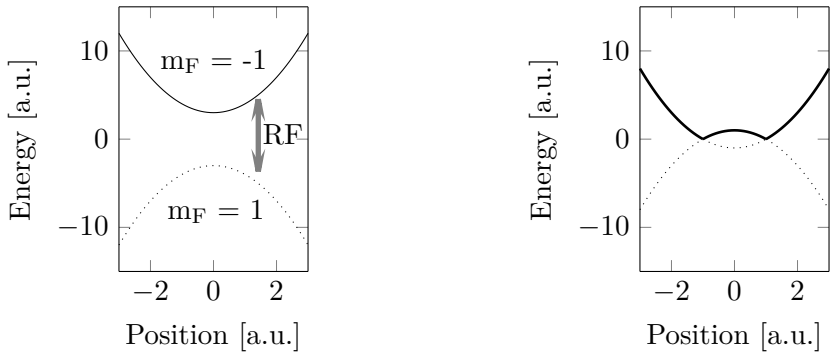

FIGURE 3.2: Principle of RF dressing: (**left**) two magnetic substates are coupled by a magnetic RF field. (**right**) The eigenenergies of the dressed states form new potential minima. Image adapted from [51]

3.2 Experimental Cycle

The preparation of the BEC takes place in a single vacuum chamber containing the atom-chip with viewports for the magneto-optical trap (MOT), optical pumping and imaging beams. Two laser sources are used, one for each of the transitions between the hyperfine ground states ($5^2s_{1/2}$, F=1 and F=2) and the excited state ($5^2p_{3/2}$) of ^{87}Rb. The lasers are locked through Doppler-free saturation spectroscopy setups. The frequency shifts needed to address the different hyperfine states (F'=(0,)1,2,3) of the excited state $5^2p_{3/2}$ are achieved with Acousto-Optic Modulators (AOMs). The energy level scheme of ^{87}Rb with the relevant optical transitions for our experiment are shown in Figure 3.3

Magneto-optical trapping The experimental sequence starts by collecting and precooling atoms in a MOT [41]. Instead of the usual MOT configuration with six MOT beams and a quadrupole field, a mirror U-MOT as described in reference [62] is implemented: Two beams are replaced by reflections from the chip surface. The magnetic field is created by U-shaped copper wires (see Figure 3.4) together with an external bias field. The MOT is loaded from background gas, where the Rubidium vapor pressure is increased by sending current through thermal dispensers. The atoms are optically cooled [36, 41] with light red-detuned ($\sim$ 20 MHz) from the cycling transition $|F = 2\rangle \leftrightarrow |F' = 3\rangle$ ('cooler'). Repumper light resonant with the $|F = 1\rangle \leftrightarrow |F' = 2\rangle$ transition brings the atoms into the cycling transition. In the MOT $\sim 10^8$ atoms are cooled to T $\simeq$ 200 μK in 18 s. [44]

Sub-Doppler cooling After the MOT is loaded, it is moved closer to the chip and compressed to match the position and size of the first magnetic trap. The magnetic fields are switched off and the detuning from the cycling transition is increased (to $\sim$ - 70 MHz) for polarization gradient cooling [41]. Due to high losses in the optical molasses the duration of this stage is short ($\sim$ 4 ms [9]).

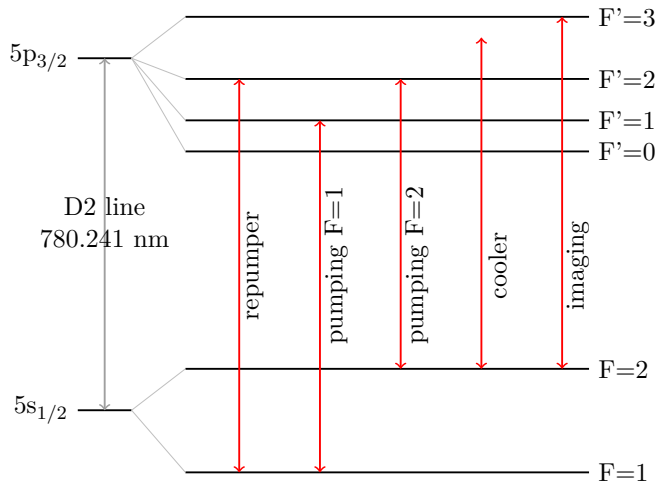

FIGURE 3.3: Hyperfine structure of Rubidium 87 (D2 line) with transitions used for cooling, optical pumping and imaging in the experiment. Image adapted from references [4, 9]. Exact values for the hyperfine splittings are given in [54].

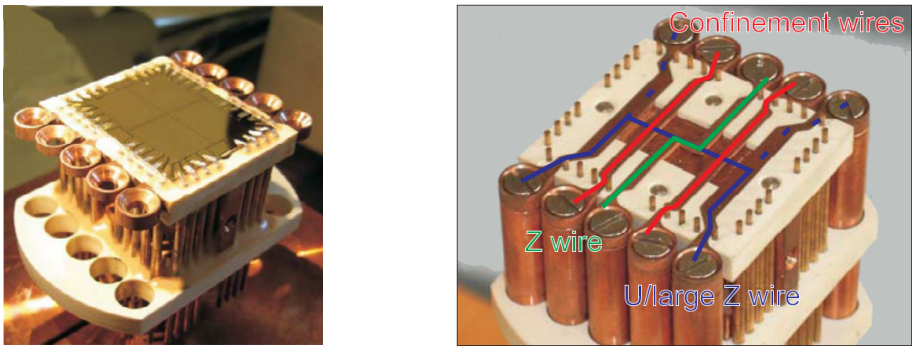

FIGURE 3.4: (**Left**) atom chip with gold surface and micro-wires. (**Right**) copper structures under the the chip. The Z-wire (green) is used for magnetic trapping after the molasses stage, the U-wire (blue) for the MOT stage and as an antenna for the RF radiation used for evaporative cooling. Either of the straight wires (red) can be used to create a field gradient for Stern-Gerlach separation of spin states in tof [4]. Image adapted from [9].

Optical pumping to $|1,-1\rangle$ At this point the atoms are in different spin states within the $|F=2\rangle$ hyperfine manifold. To optically pump them into the desired $|1,-1\rangle$ state a weak magnetic field along x that defines the quantization axis is applied and two pump beams irradiate the atoms:
A circularly polarized beam resonant with the $|F=2\rangle \leftrightarrow |F'=2\rangle$ transition ('pumping F=2') brings the atom into the $|F=1\rangle$ state . A second pump beam resonant with $|F=1\rangle \leftrightarrow |F'=1\rangle$ ('pumping F=1') irradiates the atoms along x with σ^- polarization with respect to the quantization axis. The transition rules for σ^- polarization imposes $\Delta m=-1$ for the excitation, so after many cycles of excitation and spontaneous decay (where $\Delta m=-1,0,1$) the atoms will accumulate in $|1,-1\rangle$ where they are dark to both pumping beams.

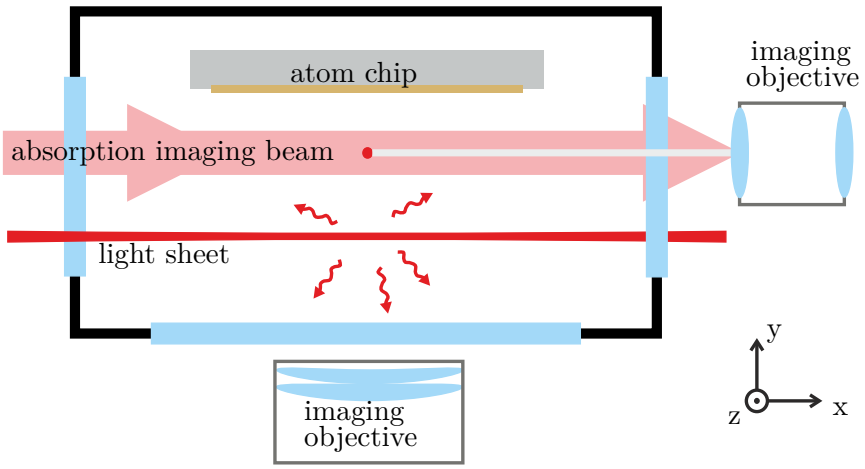

FIGURE 3.5: Sketch of the imaging systems: The absorption imaging system images along x and records the shadow cast by the atomic cloud. The fluorescence imaging system images the atoms from below, along y, by collecting photons the atoms emit when passing through the light sheet. Figure adapted from [4].

Magnetic trapping and evaporative cooling Now the atoms are cold enough and in the right state to be trapped purely magnetically and further cooled by evaporative cooling. The first magnetic trap is created by a Z-shaped copper wire (Figure 3.4) under the chip together with external fields along x ($\mathbf{B}_b$) and $-z$ ($\mathbf{B}_0$) direction. The Z-trap first matches the position and size of the optical molasses and is then compressed to match the chip trap. After compressing the trap the atoms are further cooled to degeneracy by evaporative cooling. Evaporative cooling relies on removing atoms from the cloud by inducing spin flips to an untrapped state with a 'RF-knife'. In a simplified picture, atoms with high energies are removed and the system rethermalizes to a lower temperature by collisions between atoms. A detailed description of the evaporative cooling ramp is given in [4].

After this preparation cycle, the Bose-Einstein condensates, typically containing a few thousand atoms, are ready for manipulation with various radiation fields (e.g RF-dressing to split them in double well potential as described before or coupling to other internal states as described in the next chapter) before they are imaged in tof with one of the imaging systems described below.

3.3 Imaging Systems

As in most of the ultracold atom experiments, experimental outcomes in the Rb2 experiment are probed by 'taking photographs' of the atomic cloud. Two independent imaging systems are implemented in the experiment: an absorption imaging system that images the atoms in the (y, z) plane and a fluorescence imaging system imaging in the (x, z) plane. Both image the atoms in tof after switching off the trap, which means that for each experimental cycle the atomic cloud can only be imaged once. Figure 3.6 shows images taken

with both of the systems. The atoms are imaged with light resonant with the $|F = 2\rangle \leftrightarrow |F' = 3\rangle$ transition ('imaging'), which means that the atoms have to be pumped to the $|F = 2\rangle$ state before the imaging.

3.3.1 Absorption Imaging

With the absorption imaging system we can measure the density of the atom cloud integrated over the radial imaging axis x. The atoms are illuminated with a σ^+ polarized imaging beam resonant with the $|2, 2\rangle \leftrightarrow |3, 3\rangle$ transition and the shadow cast by the atoms is recorded by a charge coupled device (CCD) camera. Each atom scatters a few hundred photons and attenuates the imaging beam. By comparing the intensity of the imaging beam $I_i(y, z)$ to the intensity of the light that passed through the cloud $I_f(y, z)$, the density of the atom cloud can be inferred from Beer-Lambert's law:

$$\frac{I_f(x, y)}{I_i(x, y)} = \mathrm{e}^{-\sigma_0 \cdot n(y,z)} \tag{3.8}$$

where $n(y, z) = \int n(\mathbf{r})\mathrm{d}x$ is the density of the cloud integrated over x and σ_0 the resonant scattering cross section of the used transition. For the chosen imaging transition $|2, 2\rangle \leftrightarrow |3, 3\rangle$, the resonant scattering cross section is $\sigma_0 = 2.91 \cdot 10^{-9}\mathrm{cm}^2$.

During each cycle four images are taken: The first containing signal from both the atoms and the imaging beam (I_f), the second tens of ms after the first to allow the atoms to leave the imaging region, and recording only the signal of the imaging beam (I_i). After reading out the camera two more images are taken without imaging beam. This allows to correct the images for stray light and background signal of the camera.

Due to the orientation of the imaging axis the absorption imaging system cannot capture transverse features of the atomic cloud such as interference fringes created by a split BEC in a double well potential [5]. It is mainly used for calibration and atom number measurements and most of the 'actual results' are obtained with the fluorescence imaging system described below.

3.3.2 Fluorescence Imaging

As sketched in Figure 3.5, the fluorescence imaging system images the atoms along y in the (x, z) plane. It is also referred to as *light sheet*, since it is created by two counter-propagating laser beams with a vertical waist of $\sim 20\mu$m. It is located ~ 1 cm under the chip surface which corresponds to a tof of 46 ms for the atoms. Contrary to the absorption imaging system where the tof can easily be adjusted between 2 and 25 ms, changing the tof for this system implies realignement of the optical paths and refocusing of the camera, therefore we work with fixed tofs of 46 ms. The atoms fall through the light sheet where

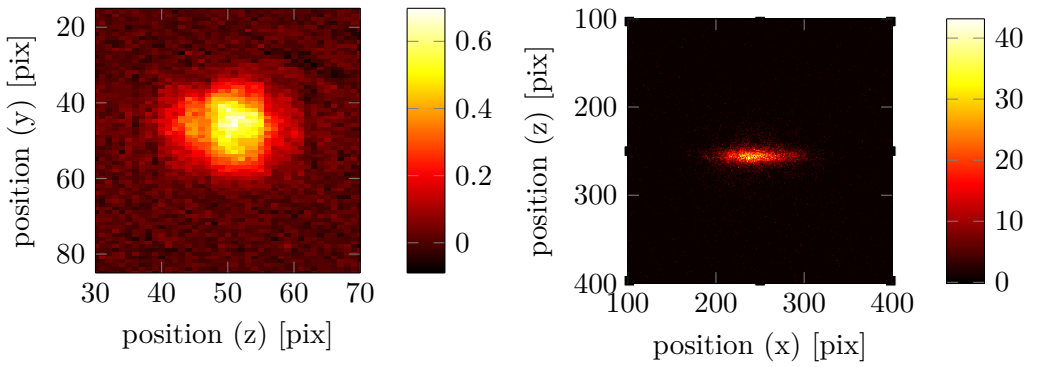

FIGURE 3.6: Exemplary images taken with the absorption imaging system (1 pix $\hat{=}$3.44μm)after 6 ms tof and the fluorescence imaging system (1 pix $\hat{=}$4μm) after 46 ms tof.

each of the atoms spends $\sim 100\mu s$ and scatters ~ 1000 photons. The camera, an electron multiplying CCD (EMCCD) camera detects about 2 % of the scattered photons, which corresponds to a sensitivity of 15 detected photons per atom.

3.4 Bose-Einstein Condensates

After having described how BECs are prepared in the Rb2 setup, I will now give a brief theoretical description of Bose-Einstein condensates, restricted to a mean-field description of BECs in harmonic trapping potentials. A description of Bose-Einstein condensates in a double-well potential based on the Bose-Hubbard model can for example be found in reference [4].

The phenomenon of Bose-Einstein condensation was first described in 1924 by S. Bose and A. Einstein. They predicted that below a critical temperature, non-interacting Bosons will macroscopically occupy the energy ground state of a given system. [42] This phase transition occurs for

$$n\lambda_{th}^3 \simeq 2.612 \tag{3.9}$$

where n is the particle density and $\lambda_{th} = (2\pi\hbar^2/mk_BT)^{1/2}$ the thermal deBroglie wavelength for particles with mass m and temperature T. Physically, this condition means that a BEC starts to form when the size of the single particle wavefunction is in the order of the inter-particle spacing $n^{1/3}$.

We consider neutral atoms confined in a harmonic potential:

$$V_{\text{ext}} = \frac{1}{2}m\left(\omega_x^2x^2 + \omega_y^2y^2 + \omega_z^2z^2\right) \tag{3.10}$$

where m is the mass of the atom and ω_i are the trapping frequencies in the three spatial directions.

The energy ground state for a single particle in a harmonic trap is that of an anisotropic

harmonic oscillator: [42]

$$\Psi_0(\mathbf{r}) = \left(\frac{m\bar{\omega}}{\pi\hbar}\right)^{3/4} \mathrm{e}^{-\frac{m}{2\hbar}\left(\omega_x^2 x^2+\omega_y^2 y^2+\omega_z^2 z^2\right)} \tag{3.11}$$

where $\bar{\omega} = (\omega_x\omega_y\omega_z)^{1/3}$ is the geometrical mean of the three trapping frequencies ω_i. We can introduce the wave function describing the state of N non-interacting Bosons as product state $\phi(\mathbf{r}) = \sqrt{N}\Psi_0(\mathbf{r_i})$ [42]. The condensate density distribution is $n(\mathbf{r}) = |\phi(\mathbf{r})|^2 = N|\Psi_0(\mathbf{r})|^2$. For non-interacting particles, the condensate size is therefore independent of the particle number N and its size can be characterized by the harmonic oscillator length $a_{ho} = \sqrt{\hbar/m\bar{\omega}}$.

Quantum scattering theory describes collisions between two identical Bosons as isotropic scattering events [42]. They are characterized by the s-wave scattering length a_s, and for average inter-particle spacings much larger than the scattering length, i.e $na_s^3 \ll 1$ we can model weak atomic interactions by an effective potential $U(\mathbf{r}) = g\delta(\mathbf{r}-\mathbf{r}')$ with a coupling constant $g = 4\pi a_s/m$.
The time evolution of such a weakly interacting gas is described by a nonlinear Schrödinger equation, the Gross-Pitaevskii equation (GPE):

$$\mathrm{i}\hbar\frac{\partial}{\partial t}\Phi(\mathbf{r},t) = \left(\frac{-\hbar^2}{2m}\nabla^2 + V_{\mathrm{ext}} + g|\Phi(\mathbf{r},t)|^2\right)\Phi(\mathbf{r},t) \tag{3.12}$$

where the inter-particle interactions are treated as a potential term proportional to the BEC density $|\Phi(\mathbf{r},t)|^2$. The groundstate for a given harmonic trap is a stationary solution of Equation 3.12 and can be found by setting $\Phi(\mathbf{r},t) = \mathrm{e}^{-\mathrm{i}\mu t/\hbar}\phi(\mathbf{r})$, where μ is the chemical potential. [16] With this, the GPE is

$$\mu\phi(\mathbf{r}) = \left(\frac{-\hbar^2}{2m}\nabla^2 + V_{\mathrm{ext}} + g|\phi(\mathbf{r})|^2\right)\phi(\mathbf{r}) \tag{3.13}$$

For a large number of atoms and repulsive interactions, the kinetic energy term is small compared to the others. In the Thomas-Fermi approximation, the kinetic energy term is dropped and a solution to Equation 3.13 can be found [42]. The density is given by: [16]

$$n(\mathbf{r}) = |\phi(\mathbf{r})|^2 = \frac{1}{g}\left[\mu - V_{\mathrm{ext}}\right] = n_0\left(1 - \frac{x^2}{R_x^2} - \frac{y^2}{R_y^2} - \frac{z^2}{R_z^2}\right) \tag{3.14}$$

where $n_0 = \mu/g$ is the peak density and R_i the Thomas-Fermi radius defined below. The density distribution described by Equation 3.14 is an inverted parabola in each direction, defined by $V_{\mathrm{ext}}(\mathbf{r})$. For $V_{\mathrm{ext}}(\mathbf{r}) = \mu$, the density is zero and the extension of the BEC is in

each spatial direction is defined by the Thomas-Fermi radii:

$$R_i^2 = \frac{2\mu}{m\omega_i^2} = a_i^2 \frac{2\mu}{\hbar\omega_i} \tag{3.15}$$

where a_i is the harmonic oscillator length given by $a_i = \sqrt{\hbar/m\omega_i}$. By normalizing the wave function to the atom number N, a value for the chemical potential μ can be found:[42]

$$\mu = \frac{\hbar\bar{\omega}}{2}\left(\frac{15Na_s}{a_{ho}}\right)^{2/5} \tag{3.16}$$

Elongated traps On the Rb2 experiment highly anisotropic trapping geometries are usually used, i.e traps with high aspect ratios up to $\omega_\perp/\omega_z \sim 300$ [4], where $\omega_\perp = (\omega_x\omega_y)^{1/2}$ is the transverse trapping frequency.

For the experimental data shown in the next chapter, we use traps with an aspect ratio of $\omega_\perp/\omega_z \sim 100$, traps which are highly confined in the transverse direction, $\omega_\perp/2\pi \sim 2$ kHz, and weakly confined longitudinally, $\omega_z/2\pi \sim 20$ Hz. For $N \sim 5000$ atoms and with Equation 3.16 the chemical potential is $\mu \sim \mathrm{h} \cdot 1$ kHz.
Condensates in such elongated traps are usually referred to as being in the 1D regime. The particles are in the transverse groundstate but populate many longitudinal modes. As their mean-field interaction energy or chemical potential is small compared with the radial level spacing, $\mu \ll \hbar\omega_\perp$, the condensates' transverse degrees of freedom are frozen.

A way to describe the shape of 1D condensates within the mean-field approximation is by assuming that the radial and longitudinal degrees of freedom are decoupled [4, 42] and the wavefunction can be written as $\phi(\mathbf{r}) = \psi(\rho)\varphi(z)$.
If the interaction energy is small compared to the radial level spacing, $\mu \ll \hbar\omega_\perp$, the intereactions between the atoms can be neglected and the transverse wavefunction can be approximated by a Gaussian, the non-interacting ground state for the radial harmonic potential $V_\perp = m\omega_\perp^2\rho^2/2$. [42]

$$\psi(\rho) = \frac{1}{\pi^{1/4}a_\perp^{1/2}}\mathrm{e}^{-\rho^2/2a_\perp^2} \tag{3.17}$$

For the axial direction, as $\mu > \hbar\omega_z$, the Thomas-Fermi approximation may be used to find the longitudinal ground state wavefunction

$$\varphi(z) = \sqrt{\frac{\mu_{1D}}{g_{1D}}} \cdot \sqrt{1 - \left(\frac{z}{R_{1D}}\right)^2} \tag{3.18}$$

The effective interaction parameter in 1D g_{1D} is obtained by rescaling the interaction constant g by averaging over the transverse density profile, such that $g_{1D} = g/2\pi a_\perp^2 = 2\hbar\omega_\perp a_s$ [48]. The effective chemical potential μ_{1D} is obtained by subtracting the ground state energy $E_\perp^0$ of the transverse wave function from the chemical potential, $\mu_{1D} = \mu - E_\perp^0$

[4]. The longitudinal Thomas-Fermi radius in the 1D regime is

$$R_{1D} = \left(\frac{3g_{1D}N}{2m\omega_z^2}\right)^{1/3} \tag{3.19}$$

The size of elongated condensates can therefore be be characterized by the transverse harmonic oscillator length $a_\perp$ and the longitudinal Thomas-Fermi radius R_{1D}. For typical experimental parameters within this thesis, $a_\perp \simeq 0.25\mu$m and $R_{1D} \simeq 25\mu$m.

A detailed description of one-dimensional quasi condensates can for example be found in [48].

4 Output coupling test: MW and RF output coupling

As stated in the introduction (chapter 1), this thesis documents the first steps towards the realization of a probing scheme that allows to investigate properties of the same BEC at different points in time. We want to do this by coupling a small fraction of atoms to a magnetically untrapped state, i.e a state with magnetic moment $m_F = 0$ of the electronic groundstate. Atoms in these states are to first order insensitive to magnetic fields and therefore leave the magnetic trap and can be imaged independently from the remaining cloud of ultracold atoms. We want to use output coupling to realize a multiple probing scheme for the investigation of the dynamics of the relative phase of BECs confined in double well potentials and to study the measurement back-action on the quantum system.

In the Rb2 experiment two systems that can couple the trapped $|1,-1\rangle$ state to an untrapped state are already integrated: First, we can use the same RF source as for evaporative cooling to couple the trapped atoms in $|1,-1\rangle$ to the untrapped $|1,0\rangle$ Zeeman substate. Second, a home-built microwave antenna [34] provides microwave (MW) radiation that can couple the trapped to the untrapped $|2,0\rangle$ state.[1] A third system, the Raman laser system described in chapter 5, couples the trapped state to the $|2,0\rangle$ state with two-photon transitions and is ready to be integrated into the experiment.

By testing output coupling with the two systems already implemented, we learn which prospects and challenges lie ahead for the realization of multiple probing schemes with the Raman laser system. The MW field and the fields created by the Raman laser system couple atoms to the same (internal) state, with the key difference of a significant momentum transfer in the case of Raman output coupling.

In this chapter, we present the results obtained when output coupling from BECs confined in single well and double well potentials with MW or RF radiation. We measured the MW coupling strength for the powers currently available in our setup. Extracting the relative phase of split condensates in a double well potential from interference fringes formed by output coupled atoms could not yet be achieved. The challenge is that the clouds of atoms in the $|2,0\rangle$ ($|1,0\rangle$) state are (de)focused, which we attribute to an effective 'magnetic lens' effect due to the second order Zeeman shift in the trapping fields.

[1] 'Radiofrequency' refers to radiation with a frequency in the order of 1 MHz, i.e comparable to the linear Zeeman shift of the magnetic substates in the ^{87}Rb groundstates for a weak magnetic field (0.7 MHz/G)[54]. 'Microwave' radiation refers to frequencies in the order of the hyperfine splitting of the groundstate ($\sim$ 6.83 GHz)

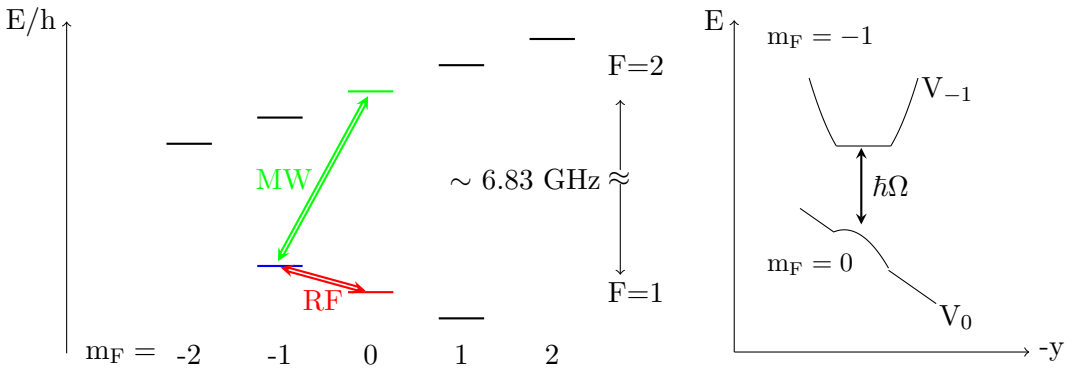

FIGURE 4.1: **left**: Energy level diagramm of the ^{87}Rb groundstate with trapped $|1,-1\rangle$ state highlighted in blue and untrapped $|2,0\rangle$ ($|1,0\rangle$) state highlighted in green (red). The trapped state can be coupled to the $|2,0\rangle$ state with MW radiation and to the $|1,0\rangle$ state with RF radiation. **right:** Sketch of the potentials for magnetically trapped and untrapped states. The magnetically trapped $|1,-1\rangle$ state experiences the potential of the harmonic trap and the mean-field potential of the condensed atoms (V_{-1}). The output coupled atoms experience the gravitational potential (gravity along y) and the mean-field potential of the still trapped BEC(V_0) Adapted from [7].

4.1 Measurement of the MW coupling strength

We use two methods to measure the coupling strength or Rabi frequency attainable with the radiation provided by the MW antenna already integrated into the Rb2 experiment:

- by scanning the MW pulse duration at constant amplitude and frequency we can extract the coupling strength from a model based on damped Rabi oscillations in a two-level atom.
- by sweeping the MW frequency through resonance at different constant sweep rates at constant amplitude we can infer the coupling strength from the Landau-Zener parameter which relates the coupling strength to the sweep rate [37].

A detailed description of the microwave antenna that provides the MW radiation we use to output couple the atoms is given in [34]. In the following we characterize the frequency of the MW field ν_{MW} with the detuning Δ_{MW} from the hyperfine splitting ΔE_{hfs} of the ^{87}Rb ground state such that

$$\Delta_{MW} = \Delta E_{\mathrm{hfs}}/\mathrm{h} - \nu_{MW} \tag{4.1}$$

Double well potential The double well potential used to obtain the results within this chapter was created by RF-dressing (see subsection 3.1.2) the trap with a dressing amplitude of $\mathrm{rf}_{\mathrm{amp}} = 0.65$ in a 'splitting time' of 10 ms. These settings were chosen because they provide double well potentials that usually give a high contrast in the interference fringes. More details on double well potentials created in our experiment can be found in references [5] and [4].

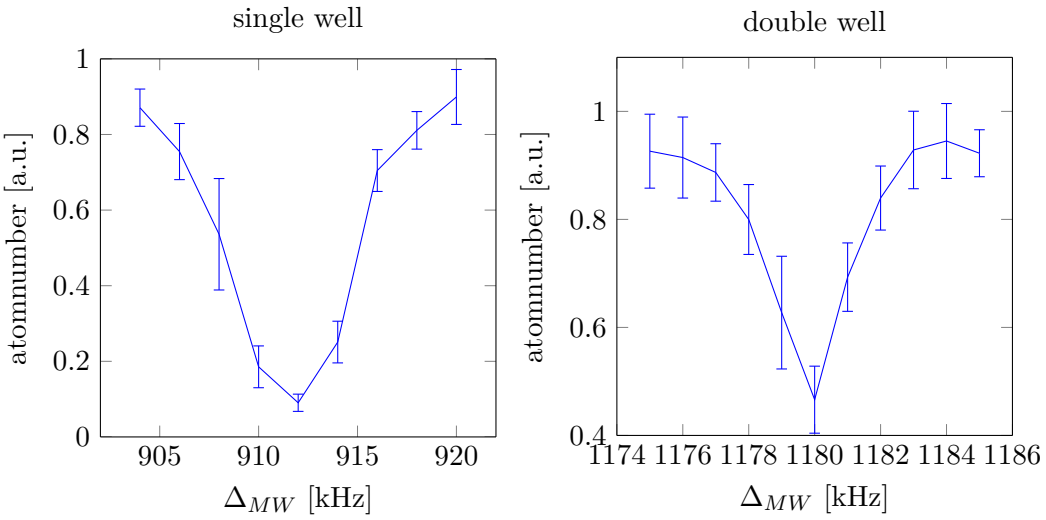

FIGURE 4.2: Trap bottom spectroscopy for **left** single well potential and **right** double well potential. The MW frequency ν_{MW} is defined w.r.t the hyperfine splitting of the ^{87}Rb ground state ΔE_{hfs}, such that $\Delta_{MW} = \Delta E_{\text{hfs}}/\text{h} - \nu_{MW}$. (MW amplitude: mw_ amp = 25, pulse duration t = 2 ms.)

Trap bottom spectroscopy The resonance frequency is identified by scanning the frequency of the MW field and looking at the atoms remaining in the $|1,-1\rangle$ state. At resonance, a maximum amount of atoms is coupled to the untrapped $|2,0\rangle$ state. To avoid power broadening we use a small MW amplitude.

4.1.1 Time scan

The first method to measure the coupling strength simply relies on scanning the MW pulse duration at maximum amplitude. The MW frequency is at resonance, as measured by the trap bottom spectroscopy above. After shining the MW output coupling pulse onto the atoms we wait for 2 ms before switching off the trap. We then image the output coupled and released cloud after 6 (8) ms tof with the absorption imaging system described in chapter 3. Figure 4.3 shows exemplary absorption images taken with varying MW pulse duration. The holding time of 2 ms is sufficient to spatially separate the output coupled cloud from the cloud released after switching off the trap. As expected, the lower, output coupled cloud becomes brighter with increasing MW pulse duration.

Figure 4.4a and Figure 4.4b show the dependence of the atom number in the trapped $|1,-1\rangle$ and untrapped $|2,0\rangle$ states on the MW pulse duration. We do not see oscillations in the relative atom numbers but rather a saturation of the fraction of output coupled atoms. As the output coupled atoms leave the trap, we can model this with damped Rabi oscillations. Comparing the experimental results to the theoretical description of damped Rabi oscillations (chapter 2), we can already estimate that the coupling strength is in the same order of magnitude as the damping accounting for the loss of atoms in the untrapped state as they leave the trap.

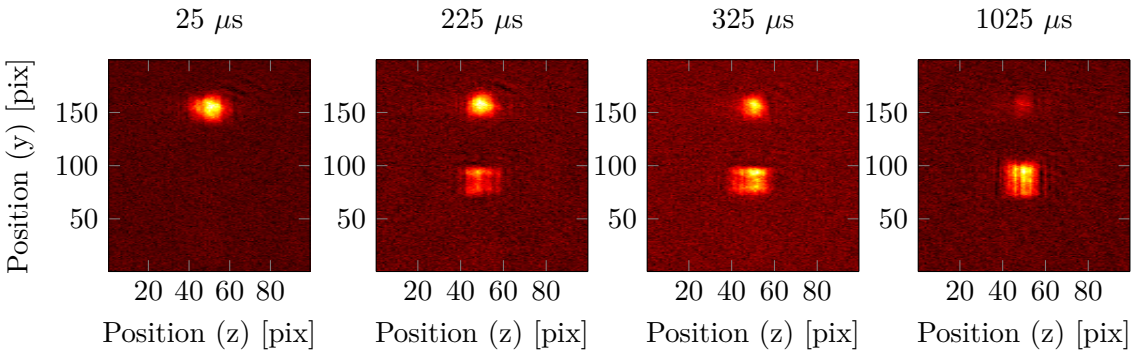

FIGURE 4.3: Examplary absorption images (single shot) taken after MW irradiation of varying pulse duration. The atom number in the untrapped state (lower region) increases with increasing pulse duration. 1 pix $\hat{=}3.44\mu$m.

4.1.2 Fit models for the evolution of the untrapped population

When subjected to the output coupling pulse, the state of each atom, originally in the trapped state, evolves into a superposition of trapped and untrapped states. In chapter 2 we calculated the time-dependent probability for a two-level atom to get transferred to an excited state when interacting with a light field close to resonance with an atomic transition. We can use this model to extract the Rabi frequency or coupling strength from our experimental data.

Beginning with a model based on the expression for damped Rabi oscillations in a two level atom as derived in chapter 2, we can equate the probability to be in the excited state $|c_e(t)|^2$ with the fraction of output coupled atoms $u(t)$. As we are coupling two long-living ground states with the MW pulse, here the damping rate γ does not model spontaneous emission but rather a phenomenological decay rate accounting for the time in which the output coupled atoms leave the trap.

$$u(t) = |c_e(t)|^2 = \frac{1}{2(1+\xi^2)} \cdot \left\{ 1 - \left[\cos(\Omega' t) + \frac{3\xi}{\sqrt{4-\xi^2}} \sin(\Omega' t) \right] \exp\left(-\frac{3\gamma t}{2} \right) \right\} \tag{4.2}$$

where $\xi = \gamma/\Omega$ is the ratio between damping rate γ and coupling strength Ω. The effective coupling Ω' is given by $\Omega' = \Omega\sqrt{1 - \xi^2/4}$.

In a second approach, we modify Equation 2.16 describing (undamped) Rabi oscillations in a two-level atom. To account for the time in which the output coupled atoms leave the trap, we include an escape time t_{esc} that models a damping mechanism and an additional parameter P corresponding to the fraction of atoms that remain trapped.

$$u(t) = P \cdot \left[1 - \exp\left(-\frac{t}{t_{\text{esc}}} \right) \right] + \exp\left(-\frac{t}{t_{\text{esc}}} \right) \cdot \left(\frac{\Omega}{\Omega_{\text{eff}}} \right)^2 \cdot \sin^2\left(\frac{\Omega_{\text{eff}}}{2} t \right) \tag{4.3}$$

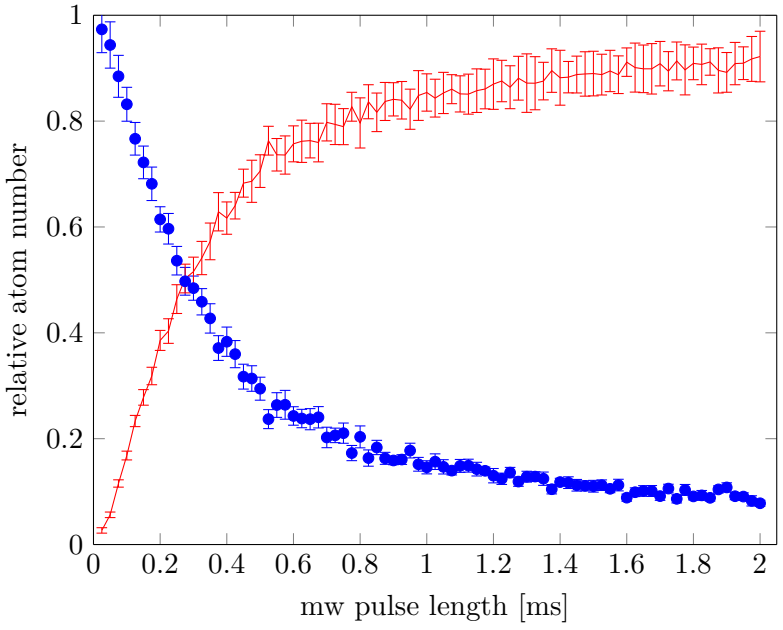

(A) **Single well:** Relative 'trapped' (blue) and output coupled (red) atomnumber as a function of the MW pulse duration. Microwave pulse with maximum available amplitude (mw_ amp=44) and a frequency defined by $\Delta_{MW} = 909$ [kHz].

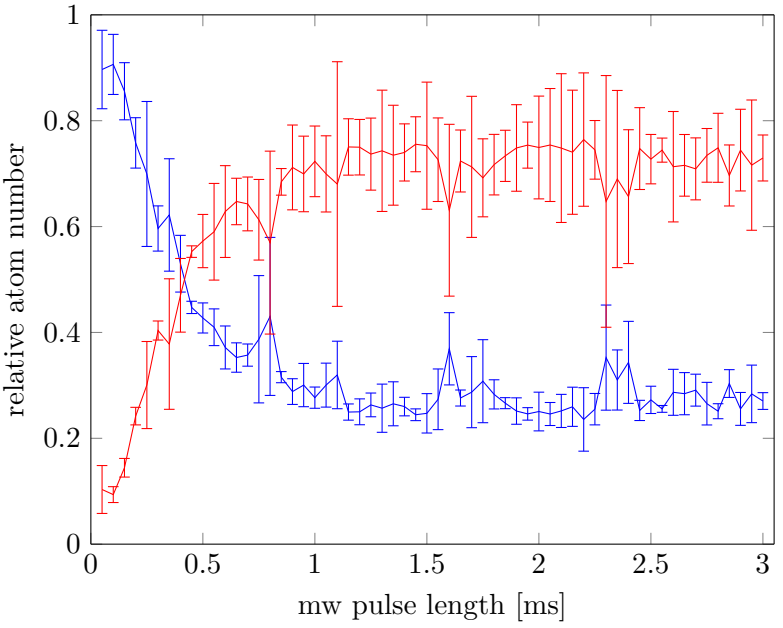

(B) **Double well:** Relative 'trapped' (blue) and output coupled (red) atomnumber as a function of the MW pulse duration. Microwave pulse with maximum available amplitude (mw_ amp=44) and a frequency defined by $\Delta_{MW} = 1180$ [kHz].

FIGURE 4.4: Relative output coupled atom number depending on MW pulse duration. Output coupling from (A) single well, (B) double well

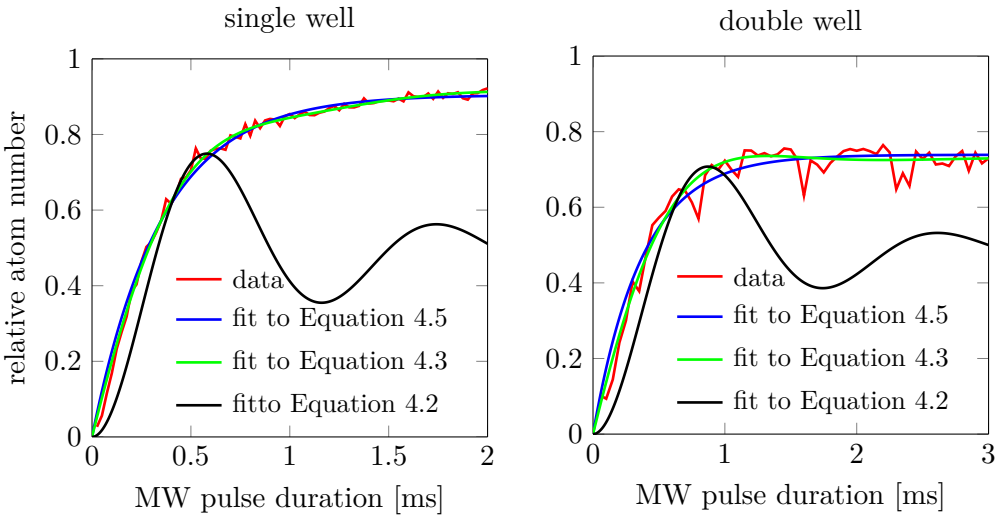

FIGURE 4.5: Fits to the output coupled fraction of atoms for BECs confined in single well and double well potentials. Blue: fit to Equation 4.5, green: fit to Equation 4.3, black: fit to Equation 4.2

Here, the effective coupling Ω_{eff} includes the detuning Δ from resonance, $\Omega_{\text{eff}} = \sqrt{\Delta^2 + \Omega^2}$. As fit parameters P, t_{esc}, Ω and Ω_{eff} are used. Δ is calculated from Ω and Ω_{eff}.

In a third model, the output coupling process is described with a rate equation. This approach is valid since the coupling strength is in the order of the output coupling rate which means that the atoms in the untrapped state leave the BEC before they flip back to the trapped state. The number of atoms in the BEC N_t evolves as [6]

$$\frac{\mathrm{d}N_t}{\mathrm{d}t} = -\Gamma \left(N_t(t) - N_0\right) \tag{4.4}$$

where $\Gamma \propto \Omega^2$ is the output rate. Solving this equation for the output coupled fraction of atoms u yields

$$u(t) = P\left(1 - \mathrm{e}^{-\Gamma t}\right) \tag{4.5}$$

where P is again the maximal fraction of output coupled atoms.

4.1.3 Results

While a fit to the data with Equation 4.2 does not converge for longer pulse durations, a fit with Equation 4.3 yields good agreement with the experimental data as shown in Figure 4.5. The results of a fit to Equation 4.3 are summarized in Table 4.1.

For a BEC confined in a single well potential the fit yields an effective Rabi frequency of $\Omega_{\text{eff}}/2\pi = 720 \pm 50$ Hz and $\Omega_{\text{eff}}/2\pi = 420 \pm 70$ Hz for double well potentials. For the

	single well	double well
atom number N	6130 ± 830	5200 ± 670
Equation 4.3		
Ω_{eff}	720 ± 50 Hz	420 ± 70 Hz
$\Omega/2\pi$	380 ± 40 Hz	320 ± 60 Hz
$\Delta/2\pi$	600 ± 60 Hz	270 ± 130 Hz
t_{esc}	0.44 ± 0.02 ms	0.51 ± 0.09 ms
P	0.92 ± 0.01	0.73 ± 0.02
Equation 4.5		
P	0.90 ± 0.01	0.74 ± 0.01
γ	2.86 ± 0.07 kHz	2.69 ± 0.25 kHz

TABLE 4.1: **Summary of results** Mean atom number and fit results for Figure 4.4a and Figure 4.4b with Equation 4.3 and Equation 4.5

data taken in a single well potential, this results in a coupling strength $\Omega/2\pi = 380 \pm 40$ Hz and $\Delta/2\pi = 600 \pm 60$ Hz. For double well potentials we extract a coupling strength $\Omega/2\pi = 320 \pm 60$ Hz and $\Delta/2\pi = 270 \pm 130$ Hz. The output coupled fraction of atoms tends to a stationary value of $\mathrm{P} = 0.92 \pm 0.01$ for single well potentials and $\mathrm{P} = 0.73 \pm 0.02$ for double well potentials. The effective escape time extracted with this model is $\mathrm{t_{esc}} = 0.44 \pm 0.02$ ms for single well potentials and $\mathrm{t_{esc}} = 0.51 \pm 0.09$ ms for double well potentials.

In contrary to Rabi oscillations in a two level atom, we are dealing with a many-body system with a width in the order of the chemical potential $\mu \simeq \mathrm{h} \cdot 1\mathrm{kHz}$. Δ should therefore be interpreted as a factor modeling the width of the BEC. Similarly, t_{esc} can be interpreted as the pulse duration for which the Fourier width of the pulse $t_{\text{esc}}^{-1} \simeq 2$ kHz is in the order of the chemical potential, i.e the entire condensate is addressed by the output coupling pulse.

4.1.4 Alternative measurement of the Rabi frequency

The atoms can also be coupled to the untrapped state by sweeping the MW frequency through resonance, by applying a MW pulse with varying frequency. We do this by choosing a fixed time window (t=1 ms) in which the frequency is ramped up linearly in time over a given frequency range. By scanning this sweep range, we get different constant sweep rates $\mathrm{d}\omega_{MW}/\mathrm{d}t$. The population in the untrapped state depends on the sweep rate and the coupling strength Ω as given by the Landau-Zener parameter Γ. With this scheme, the population in the untrapped state is given by [37]

$$\begin{aligned} u &= 1 - \exp(-2\pi\Gamma) \\ \Gamma &= \Omega \cdot \left(4\frac{\mathrm{d}\omega_{MW}}{\mathrm{d}t}\right)^{-1} \end{aligned} \tag{4.6}$$

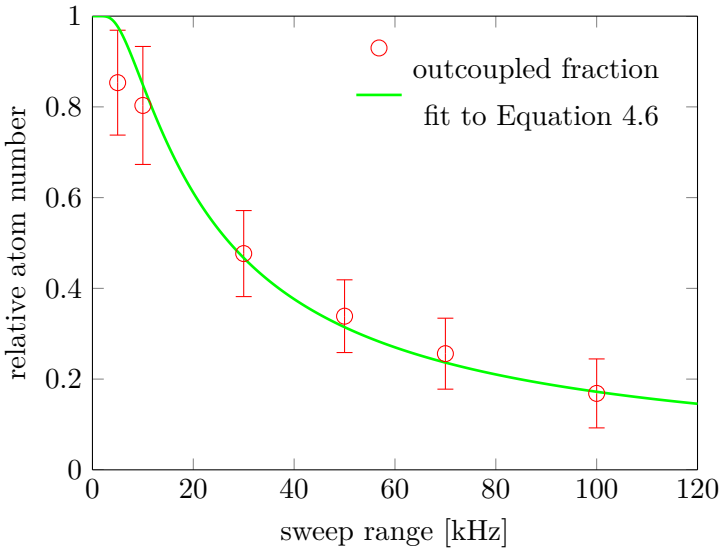

FIGURE 4.6: **Single well:** Relative output coupled atomnumber depending on the MW sweep range. Red: data, Green: fit to data with Equation 4.6. Maximum MW amplitude (mw_ amp = 44)

By this method we measured the coupling strength for a condensate trapped in a single well potential. Figure 4.6 shows the output coupled fraction of atoms depending on the sweep rate and a fit to the data with Equation 4.6. The Rabi frequency extracted by a fit to the data is $\Omega = 1.38 \pm 0.15$kHz, which is a factor 4 higher than the result obtained by varying the pulse duration.

4.1.5 Conclusion

We applied two methods to measure the Rabi frequency of the MW coupling at maximum available MW power. By scanning the MW pulse duration at a fixed frequency and amplitude we find that the coupling strength is $\Omega/2\pi \sim 300 - 400$Hz for BECs confined in single well and double well potentials. Sweeping the MW frequency through resonance results in a Rabi frequency $\Omega/2\pi \sim 1.4$kHz. A third value for the MW Rabi frequency is given in references [34, 44], where the Rabi frequency is extracted from a measurement of two-photon Rabi oscillations between the $|1,-1\rangle$ and $|2,1\rangle$ state. It yields a coupling strength $\Omega/2\pi \sim 3$kHz, which is another factor of two higher.

With the radiation provided by the MW antenna we can only achieve Rabi frequencies in the order of possible detunings and decay rates, $\Omega \sim \Delta, t_{\mathrm{esc}}^{-1}$, therefore the second method relying on frequency sweeps through resonance is certainly more reliable since it is not affected by detunings from resonance and damping rates. For much higher coupling strengths, i.e $\Omega \gg \Delta, \mathrm{t_{esc}}^{-1}$, as we expect to attain with the Raman system presented in the next chapter, scanning the pulse duration will be a suitable method to observe Rabi

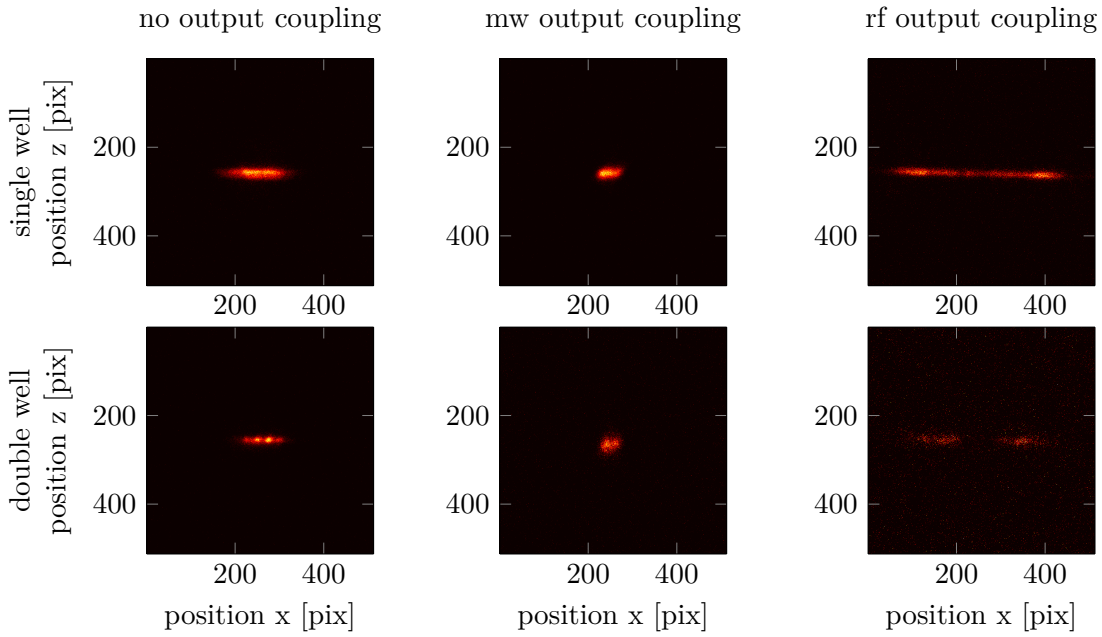

FIGURE 4.7: Exemplary fluorescence images taken **(left)** without output coupling pulse and with a **(middle)** MW output coupling pulse or a **(right)** RF output coupling pulse incident on the atoms. **Top:** single well. **Bottom:** double well. While interference fringes can be seen when switching off the trapping fields, they can not be observed in the clouds of output coupled atoms. Instead the transverse profiles are focused or broadened, depending on the internal state of the output coupled atoms. Images corrected for background noise and etaloning. Single shots, 1 pix $\hat{=}4\mu$m.

oscillations.

4.2 Spatial profiles of output coupled clouds

Information about the spatial distribution of the output coupled atoms is obtained by the fluorescence imaging system described in section 3.3. The atoms are imaged in the horizontal (x, z) plane after 46 ms tof. Figure 4.3 shows examplary fluorescence images of clouds dropped after switching off the trap, RF- and MW output coupled clouds. We can choose to image the output coupled cloud or the cloud dropped after switching off the trap by adjusting the camera trigger time. In order to spatially separate the two clouds, we use a holding time of 15 ms between applying the output coupling pulse and switching off the trapping fields. Figure 4.8 shows a scan of the camera trigger time for RF- and MW output coupled clouds, showing that we can image output coupled and dropped clouds individually by adjusting the camera trigger time as well as a (de)focusing of the output coupled clouds compared to the dropped clouds.

We could not observe interference fringes in the transverse direction when output coupling from BECs confined in double well potentials. Instead, we see a strong transverse focusing

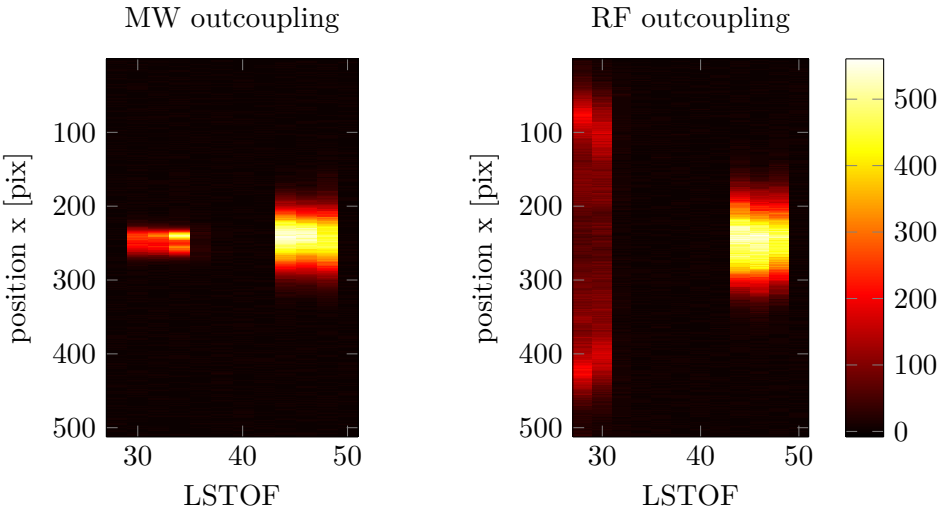

FIGURE 4.8: Scan of camera trigger time (LSTOF). Left: double well, MW output coupling to $|2,0\rangle$. Right: single well, RF output coupling to $|1,0\rangle$. LSTOF < 35 ms: atoms in $|2,0\rangle$ ($|1,0\rangle$). 42 ms $<$ LSTOF < 48 ms atoms released after trap switch off. Transverse profiles (Integrated along z), average over 5 shots, 1 pix $\hat{=}4\mu$m.

of the MW output coupled cloud in the $|2,0\rangle$ state. Its transverse width is reduced by a factor of $\sim 1.5-2$ compared to the width of a cloud released when switching off the trap. The RF-output coupled atomic cloud in $|1,0\rangle$ is defocused, its transverse profile is $\sim 2-4$ times broader than the one of the dropped cloud. This effect can be seen in single and in double well trapping potentials (see Figure 4.9) We assume that this is the main reason for not observing interference fringes because the fringes can either not be resolved or are washed out.

In the following, we will analyze this effect, which we attribute to the interaction of the output coupled atoms with the trapping fields and discuss the frequency dependence of the transverse profiles of RF- and MW output coupled clouds.

4.2.1 Effect of magnetic trapping fields

In the description of the interaction of the magnetic moment of an atom with an external magnetic field in the previous chapter (section 3.1) the second-order Zeeman shift has been neglected since it does not contribute much to the energy of the trapped low-field seeking atoms: As described in chapter 3 the atoms are trapped in regions where the magnetic field is in the order of the offset field $B_0 \sim 1$ G. For the electronic ground state of ^{87}Rb, the linear Zeeman shift is 0.7 MHz/G, while the second order shift is ~ 0.6kHz/G^2 [54], three orders of magnitude smaller than the linear Zeeman shift. For the atoms trapped in regions with weak magnetic field gradients and curvatures the second-order shift is therefore negligible. For atoms in a state $m_F = 0$ there is no linear Zeeman shift, and the interaction of the output coupled atoms with the trapping field is dominated by the second-order Zeeman shift.

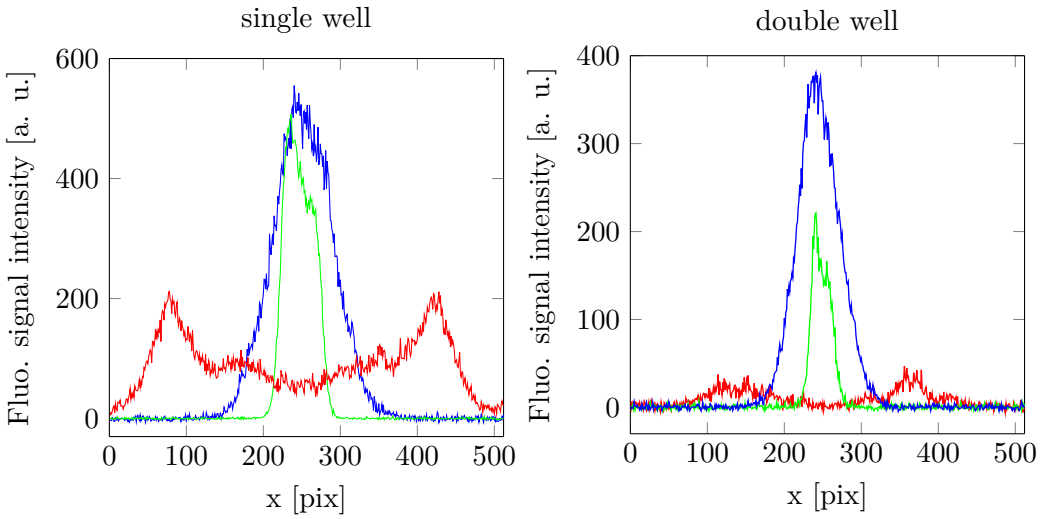

FIGURE 4.9: Averaged transverse profiles of atom clouds released after trap switch off **(blue)**, MW output coupling **(green)** and RF output coupling **(red)**. Left: Single well, right: double well. 1 pix $\hat{=}4\mu$m.

For alkalis in the groundstate the energy of an atom in an external magnetic field of magnitude B can be calculated analytically with the *Breit-Rabi formula* [8, 54]

$$E_{|\tilde{F}=I\pm J,m\rangle} = -\frac{\Delta E_{\text{hfs}}}{2(2I+1)} + g_I \mu_B m B \pm \frac{\Delta E_{\text{hfs}}}{2}\left(1 + \frac{4mX}{2I+1} + X^2\right)^{1/2}$$
$$X = \frac{(g_J - g_I)\mu_B B}{\Delta E_{\text{hfs}}} \tag{4.7}$$

Here, ΔE_{hfs} denotes the hyperfine splitting of the ground state, g_I and g_J are the Landé factors associated with the nuclear spin $\mathbf{I}$ and the total electron angular momentum $\mathbf{J} = \mathbf{S} + \mathbf{L}$, where $J = 1/2$ for alkali ground states. The Breit-Rabi formula is valid for magnetic fields for which the atom's energy shift is small compared to the finestructure splitting. For weak magnetic fields, i.e. for $B \to 0$ the eigenstates $\left|\tilde{F} = I \pm J, m\right\rangle$ are characterized by the projection of the total angular momentum $\mathbf{F}$ on the magnetic field $|F, m_F\rangle$. Note that for $|2,0\rangle$ (upper sign) the energy increases while it decreases for $|1,0\rangle$ (lower sign). This is also shown in Figure 4.10.

The force due to an inhomogeneous magnetic field is [8]

$$\mathbf{F} = -\frac{\partial E}{\partial B}\nabla B \tag{4.8}$$

Differentiating Equation 4.7 w.r.t B for $m = 0$ yields

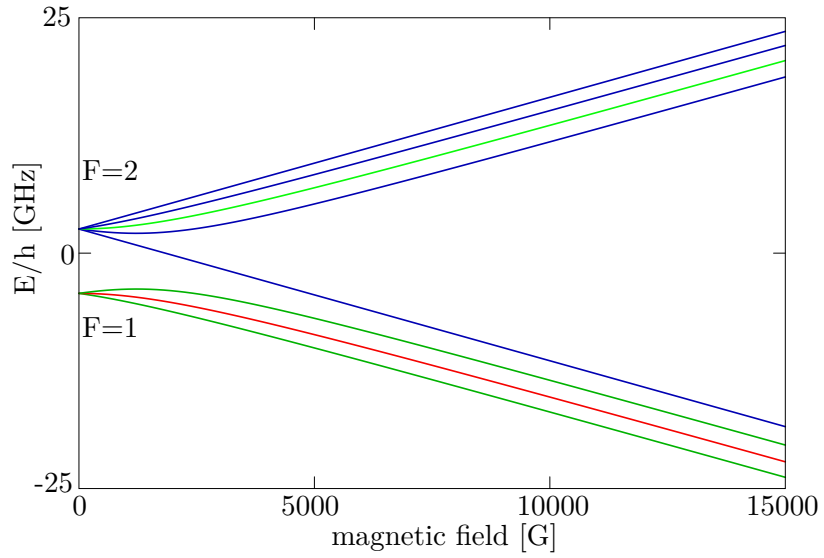

FIGURE 4.10: Level structure of ^{87}Rb in an external **B**-field. The levels highlighted in green and red correspond to states with $m_F = 0$ for weak magnetic fields. Image adapted from reference [54]

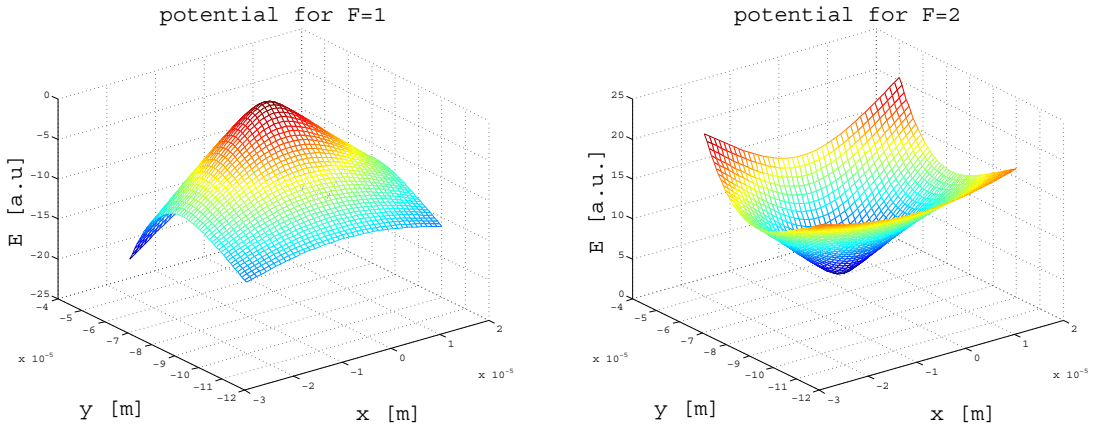

FIGURE 4.11: Effective potential as given by Equation 4.7 for **left** atoms in $|1,0\rangle$ and **right** atoms in $|2,0\rangle$.

$$\frac{\partial E}{\partial B} = \pm \Delta E_{\text{clock}} \cdot \frac{1}{\sqrt{1+X^2}} \cdot B \tag{4.9}$$

where

$$\frac{\Delta E_{\text{clock}}}{B^2} = \frac{((g_J - g_I)\mu_B)^2}{2\Delta E_{hfs}} = \text{h} \cdot 575.15\text{Hz/G}^2$$

is the second-order Zeeman shift between the two clock states for the ^{87}Rb ground state in weak magnetic fields and X as defined in Equation 4.7. [54]

With this the force along x and y is

$$\mathbf{F} = \mp \Delta E_{\text{clock}} \cdot \frac{1}{\sqrt{1+X^2}} \cdot \begin{pmatrix} B_x \partial_x B_x + B_y \partial_x B_y \\ B_x \partial_y B_x + B_y \partial_y B_y \end{pmatrix} \tag{4.10}$$

Calculation of paths of output coupled atoms The purpose of this calculation is to check whether the alteration of the width of the transverse profiles as shown in Figure 4.9 can be attributed to the force due to the second-order Zeeman shift in the inhomogeneous magnetic trapping field. The trajectories of the output coupled atoms in the transverse (x, y) plane are calculated under the influence of gravitational acceleration along y and depending on the internal state a repulsive or attractive force as described by Equation 4.10. The magnetic field was assumed to be that of an infinitely long and thin wire along z together with a homogeneous field along x as shown in Figure 3.1 in chapter 3 to approximate the transverse single well trapping potential.

The atoms' position is initialized such that they lie on a circle of radius $\sim 1\mu$m around the trap minimum. The atoms' initial velocity is $v_{in} = (2\mu/m)^{1/2}$ with $\mu = \text{h} \cdot 1$ kHz. This corresponds to the maximum kinetic energy attainable from atomic interactions when the atoms leave the trap center.

Comparison to width of transverse profiles We extracted the widths of the transverse profiles by fitting a Gaussian to the data (see Figure 4.13). Assuming a Gaussian ground state for the transverse profile, $\psi(\rho) = \frac{1}{\pi^{1/4} a_\perp^{1/2}} \text{e}^{-\rho^2/2a_\perp^2}$, the width of the cloud expanding ballisticly in tof can be estimated by $\sigma(t) = a_\perp \cdot (1 + (\omega_\perp t_{\text{exp}})^2)^{1/2}$ [32], where t_{exp} is the expansion time or tof. The fit yields a width of $\sigma(t) = 38\text{pix} \simeq 0.15$ mm which corresponds to a harmonic oscillator length of $a_\perp^{\text{meas}} = 0.26\mu$m after expansion in 46 ms tof and a transverse trapping frequency of $\omega_\perp \simeq 2\text{kHz}$, which is compatible with the calculated harmonic oscillator length $a_\perp = (\hbar/m\omega_\perp)^{-1/2} = 0.24\mu$m. The FWHM of the fitted Gaussian to the profile of the dropped cloud is $w \simeq 0.36$ mm. For the MW output coupled the fit yields a FWHM of 0.2 mm.

In the case of the RF output coupled cloud we roughly approximate the width of the profile by the distance between the two peaks, resulting in a width of 1.32 mm. In Table 4.2 the FWHMs of the Gaussian fit to the data are summarized and compared to the calculation.

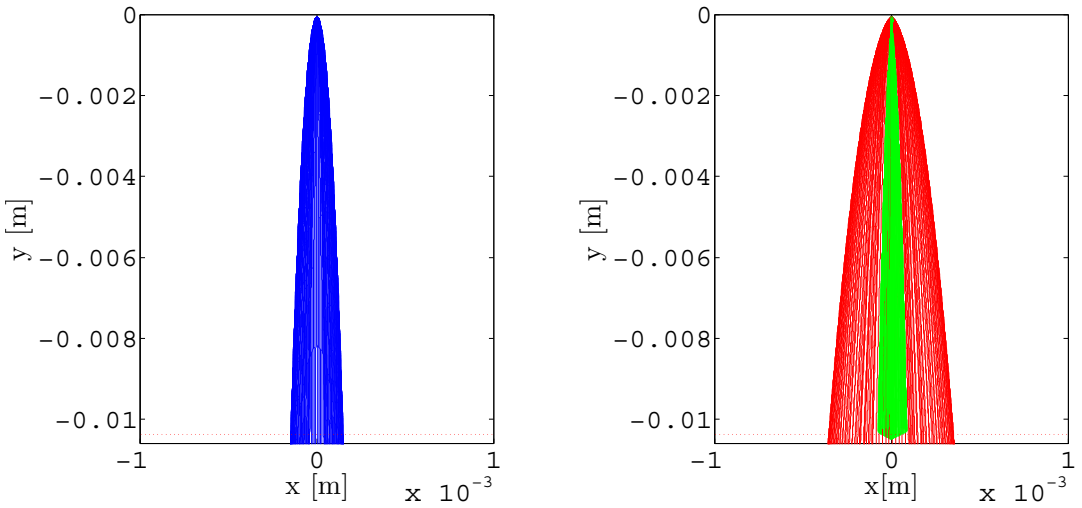

FIGURE 4.12: Paths of atoms in the (x, y) plane **(left)** without magnetic field influence, such as for atoms released after switching off the trap **(right)** for output coupled atoms in the trapping field. (Red) atoms in $|1, 0\rangle$, (green) atoms in $|2, 0\rangle$. The dashed line indicates the position of the light sheet

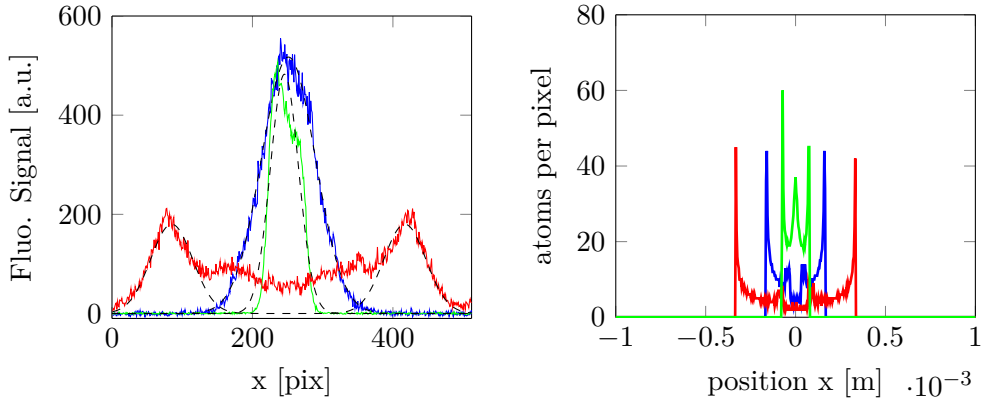

FIGURE 4.13: **left:** Averaged transverse profiles with Gaussian fit (black dashed lines) to the data to extract the width of the profiles. (**blue**) Cloud dropped after trap switch off, (**green**) MW output coupled clouds, (**red**) RF output coupled clouds. 1 pix $\hat{=}4\mu$m. **right:** Calculated paths of atoms. Contour plot of a histogram at light sheet position. The high peaks on the edges of the clouds are due to the initialisation of the calculation.

	transverse width of spatial profile (FWHM)	calculation
trap switch off	90 pix $\simeq$ 0.36 mm	0.3 mm
MW-outcoupling	50 pix $\simeq$ 0.2 mm	0.2 mm
RF-outcoupling	330 pix $\simeq$ 1.32 mm	0.7 mm

TABLE 4.2: Comparison of widths of transverse profiles to calclulation of paths of output coupled profiles

In the calculation, the second-order Zeeman shift ΔE_{clock} needs to be re-scaled by a factor of two to match the experimental observations. Figure 4.12 shows the result of this calculation. The spatial extension of the paths at the position of the light sheet agrees well with the measured widths of the MW output coupled clouds and the clouds dropped after switching off the trap.

We will see in the next section that the width of RF output coupled clouds depends strongly on the output coupling frequency. In order to model the width of the output coupled cloud precisely we would need to take both frequency and duration of the output coupling pulse into account.

Rescaling of the interaction with the trapping fields Although this simple model confirms the influence of the second-order Zeeman shift of the output coupled clouds in the trapping fields, we had to rescale the interaction by a factor of two such that $\Delta E^{\text{calc}}_{\text{clock}} = \Delta E_{\text{clock}}/2$ to match the experimental observations. Several approximations have been made in the calculation: Due to the initialization of the position of the atoms, we neglected the interaction with the magnetic field inside the BEC. Further, we neglected any interactions between the atoms expanding in tof and the finite size of the wire creating the trapping field.

A way to model our experimental observations more carefully is to numerically solve the Gross-Pitaevskii equation (Equation 3.12) for the output coupled atoms as trapped in an external anharmonic potential given by the Breit-Rabi formula (Equation 4.7) for states with $m = 0$. In solving the GPE, the interactions with the still trapped BEC can be taken into account by the mean-field potential. Additionally, with such a simulation we can check the influence of the momentum kick away from the trap center in the case of Raman output coupling on the density distribution of the output coupled atoms.

4.2.2 Spatial profile of an atom laser

As already mentioned above, the spatial transverse profile of the output coupled clouds depends crucially on the output coupling frequency (also, see Figure 4.15). Due to its finite size, the trapped BEC extends over a region with different magnetic field strengths.

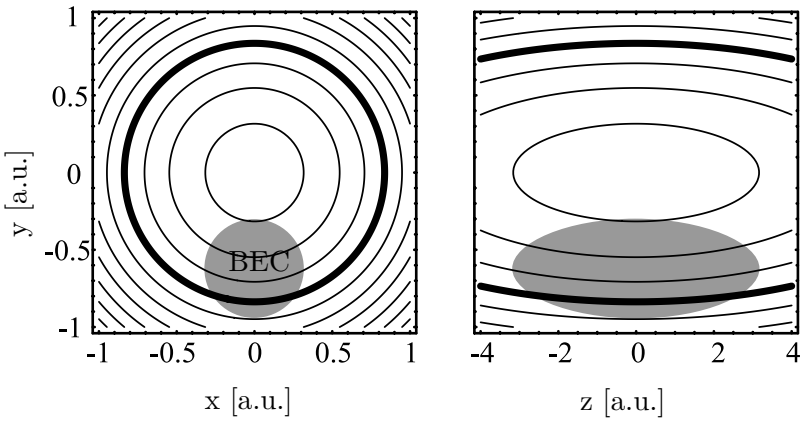

FIGURE 4.14: Sketch of output coupling resonance surface for an elongated BEC: The BEC (grey ellipsoid) extends over a spatially varying magnetic field (black contour lines). Under the influence of gravity, the condensate's center is $z_{\text{sag}} = -g/\omega_\perp^2$ below the field minimum. The thick black line indicates the region where the output coupling pulse transfers atoms to a magnetically untrapped state, the resonance surface. Left: Cut perpendicular to the long axis of the BEC, right: cut perpendicular to the transverse direction. Image adapted from [6].

The resonance frequency for spin flips from the trapped $|1,-1\rangle$ to the untrapped $|1,0\rangle$ state is given (to first order) by the linear Zeeman shift and as the magnetic field varies over the extension of the BEC, the resonance becomes position dependent. With short, broadband output coupling pulses, with a pulse duration such that the Fourier width of the pulse becomes comparable to the chemical potential of the BEC, the entire BEC can be addressed and the output coupling is spatially independent [47]. With long output coupling pulses with a narrow Fourier width, a specific spatial region within the BEC is addressed. Neglecting gravity, the resonance surface is an ellipsoid centered around the condensate. Due to the gravitational sag, the resonance surface cuts through the BEC [6, 47]. This is illustrated in Figure 4.14.

When leaving the trapping region, the output coupled atoms interact with the remaining atoms. As the mean-field potential of the trapped cloud is not homogeneous over the output coupling surface the momentum of the output coupled atoms spreads. In a classical picture, this would correspond to atoms rolling off a potential from different heights [12]. When moving the resonance surface to the center of the BEC, the mean-field potential gets stronger and transverse momentum spread and the width of the output coupled cloud larger.

The observed double peak structure is qualitatively consistent with the results presented in [12, 33, 46]. In [46] the transverse profile of an RF output coupled atomlaser is analyzed analytically by optical methods in analogy to an optical laser and in [33] and [12] the transverse profiles are modeled by numerically solving the GPE. As the output coupling frequency increases, the resonance surface moves towards the margins of the BEC where the mean-field potential is weaker and the transverse momentum spread of the output coupled

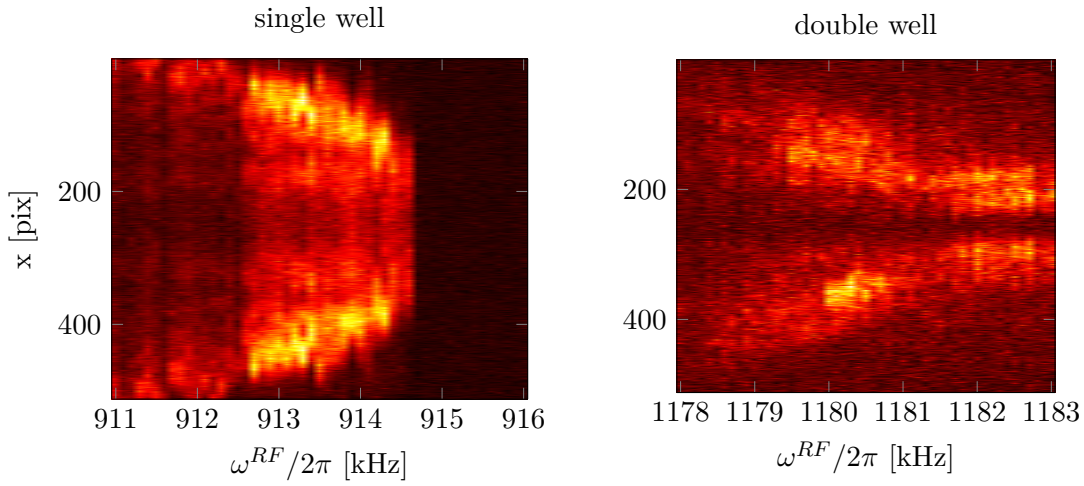

FIGURE 4.15: Scan of the output coupling frequency: (**left**) RF output coupling from a BEC confined in a single well and (**right**) from a BEC confined in a double well potential. Profiles averaged over 5 shots, constant RF-amplitude and constant RF-pulse duration ($\tau_{RF} = 5$ ms). Scan of the RF-frequency in steps of 100 Hz. 1 pix $\hat{=}4\mu$m.

atoms decreases. The signature of this effect is the decrease of the distance between the two peaks as can be seen in Figure 4.15. In principle, the two peaks should merge at high output coupling frequencies, which we do not observe.

The data was obtained by scanning the RF-frequency in steps of 100 Hz with a constant RF-amplitude and a pulse length of $\tau_{RF} = 5$ ms. The Fourier width of the pulse $\sim \tau_{RF}^{-1} =$ 200 Hz is therefore smaller than the chemical potential of the BEC and by scanning the RF-frequency, we output couple from different spatial regions within the BEC.

Profiles of MW output coupled clouds

In Figure 4.16 and Figure 4.17 the dependence of the transverse profiles of MW output coupled clouds on the MW-frequency and MW-amplitude is shown. We used a pulse duration of $\tau_{MW} = 2$ ms, the Fourier width of the pulse is therefore ~ 500 Hz. We do not observe a dependence of the transverse width of the output coupled clouds on the MW-frequency (Figure 4.16). This can be attributed to the magnetic lens which focuses the MW output coupled clouds. Further, the Fourier width of the MW-pulse is not significantly smaller than the chemical potential and therefore the frequency-dependence of the output coupled profiles cannot be resolved. In choosing a long pulse duration, such that the Fourier width of the output coupling pulse is smaller than the step size of the frequency scan, we could check whether the magnetic lens suppresses the observation of a frequency dependence of the shape of the MW output coupled profiles.

Figure 4.17 shows the amplitude dependence of the MW output coupled profiles for single and double well trapping potentials. For double well trapping potentials, we recover the expected double peak structure as described in the last section. As for now, we do not understand, why we don't observe a similar structure for clouds output coupled from a

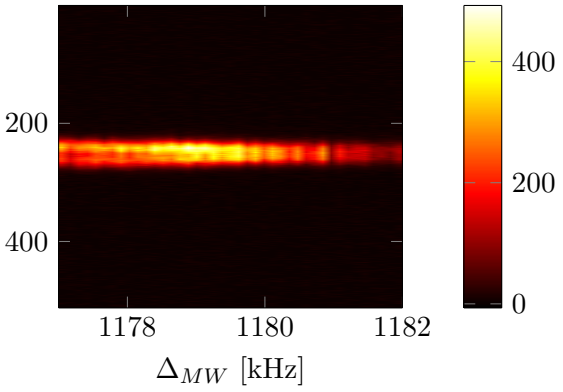

FIGURE 4.16: Transverse profiles of MW output coupled clouds (from a double well trapping potential) depending on output coupling frequency at constant MW-amplitude (mw_amp = 28) and constant pulse duration, $\tau_{MW} = 2$ ms. The MW frequency ν_{MW} is defined w.r.t the hyperfine splitting of the ^{87}Rb ground state ΔE_{hfs}, such that $\Delta_{MW} = \Delta E_{\mathrm{hfs}}/\mathrm{h} - \nu_{MW}$.

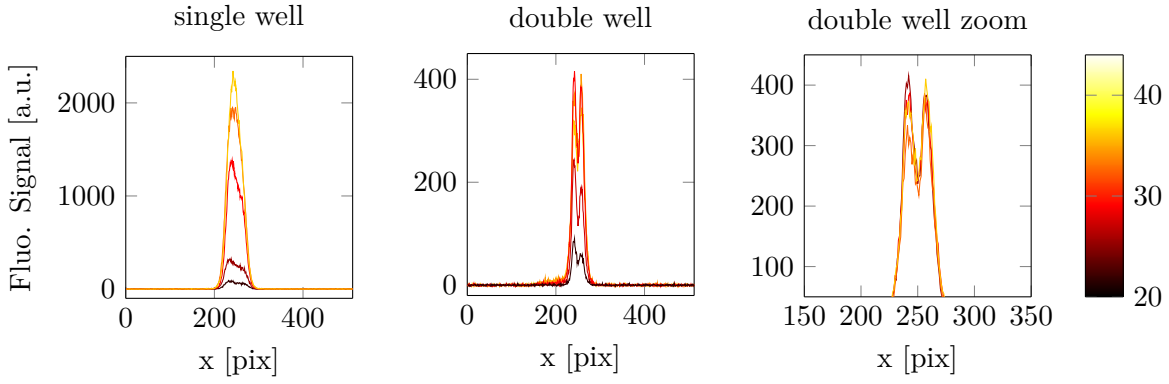

FIGURE 4.17: Averaged transverse profiles of output coupled clouds at different MW amplitudes, with constant pulse duration $\tau_{MW} = 2$ ms. (**left**) single well, $\Delta_{MW} = 912$ kHz. (**center**) double well, $\Delta_{MW} = 1180$ kHz. (**right**) zoom onto double peak structure. The colorbar indicates the MW-amplitude. 1 pix $\hat{=}4\mu$m.

single well potential. An interesting amplitude dependence of the double peak structure is observed for the clouds output coupled from a double well trapping potential: For small MW-amplitudes the left peak is higher and with increasing amplitude the higher peak flips to the right. This effect was reproducible, note that Figure 4.17 shows profiles averaged over 5 experimental realizations.

Conclusion

We now have an idea which challenges lie ahead for the observation of interference fringes from atoms output coupled from a double well trapping potential. We plan to model the magnetic lens more precisely and include the mean-field potential and output coupling frequency in our calculation by numerically solving the GPE. In the next chapter, the Raman laser system is described, with which momentum is imparted onto the output coupled atoms such that they leave the trapping region faster. Once we have a better understanding of the output coupling process including the magnetic lens, we can check whether the momentum kick away from the trapping region will suffice to observe interference fringes from atoms coupled to the $|2, 0\rangle$ state.

5 Raman laser system

In this chapter the setup of the Raman laser system is presented, the construction of which was the main goal for this master thesis. It is designed to drive Raman transitions between the $|1,-1\rangle$ and $|2,0\rangle$ states of the ^{87}Rb ground state ($5^2s_{1/2}$). The design is mainly inspired by the work done by John E. Debs [16, 17] and we expect Rabi frequencies up to 1 MHz, three orders of magnitude higher than achieved with MW coupling presented in the previous chapter.

5.1 Principle

As we have seen in chapter 2, Raman transitions require two light fields with a stable frequency difference that corresponds to the energy difference of the levels involved in the wanted transition. As we want to drive Raman transitions between two hyperfine states of the ^{87}Rb groundstate, we require two light fields with a frequency difference $\Delta\omega/2\pi = \Delta E_{\mathrm{hfs}}/h \simeq 6.83$ GHz. We want this frequency difference to be tuneable to sub kHz precision to address different energy shells within the condensate (as shown in Figure 4.14). Two laser beams with a frequency separation of $\sim$6.83 GHz can be produced by means of different methods: Two lasers relatively detuned by this frequency can be phase-locked (see e.g reference [58]) to yield a stable frequency difference. Another possibility is to modulate the laser current of a single laser which generates frequency sidebands at the modulation frequency [45]. We have implemented yet another possibility using a single laser together with an electro-optic modulator (EOM) as frequency shifting element.

As described in chapter 2, two-photon Raman transitions couple the two target states via a third level. For a coherent Raman process, this level is not populated and therefore referred to as virtual level. As we wish to suppress single photon transitions to the first excited state, each of the two laser fields should be far detuned from the ^{87}Rb D2-line. The single photon scattering rate scales as Δ^{-2} (Equation 2.24) while the two-photon Rabi frequency is proportional to Δ^{-1} (Equation 2.34). By operating the laser red-detuned by $\Delta/2\pi \simeq 100$ GHz, we can strongly suppress the single photon scattering rates and still achieve high two-photon coupling with the available laser powers.

We further require a fast switch to control the timing and pulse duration at μs precision, which we implement by using acousto-optic modulators (AOMs).

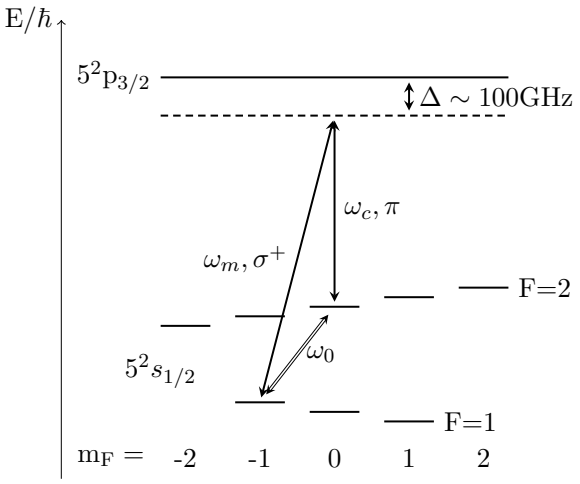

FIGURE 5.1: **Principle of Raman transitions.** Energy level scheme of ^{87}Rb with energy levels relevant for Raman transitions in our setup.

5.2 Setup

Figure 5.3 shows a scheme of our setup to drive Raman transitions. In the following part the main elements are briefly described.

Light source

We use an external cavity diode laser (ECDL)[1] in Littrow configuration operating at 780.444 nm, about 100 GHz red-detuned from the ^{87}Rb D2 line. The detuning or output frequency is tuned by adjusting the angle of the laser grating. We monitored the output wavelength regularly to 0.005 nm precision and can exclude frequency drifts greater than 2.5 GHz, the detuning is stable at least to 2.5%.

To avoid back-reflection into the laser diode, we use a polarization dependent optical isolator. In the isolator the polarization of the beam is set by an input polarizer and rotated by 45° in a magnetic field. The output polarizer is also rotated by 45° with respect to the input polarizer. Back-reflected light is blocked by the input polarizer, as its polarization is rotated by 90° with respect to the input polarization as it passes the magnetic field twice. We could only achieve a maximal transmission of $\sim 70\%$ of the optical power through the isolator right after the source due to differently polarized regions in the beam. As we can couple the beam filtered by the optical isolator efficiently into the optical fibers (typical efficiency of 50%), we still have enough output power to achieve high coupling strengths with this setup. (see section 5.3)

[1] *Toptica* DL 100

Electro-optic modulator

We use a fiber-coupled EOM [2] to generate the Raman beams with a frequency difference in the order of 6.83 GHz.

The operation of an EOM is based on the Pockels-effect, the dependence of the index of refraction of the used medium on the applied electric field. The change of the refraction index Δn depends linearly on the applied field E:

$$\Delta n = n_0^3 \cdot r \cdot E \tag{5.1}$$

for a material with refractive index n_0 and electro-optic coefficient r. Light with wavelength λ passing through a crystal of length L and thickness d will pick up a phase shift given by [59]

$$\Delta\Phi = \frac{2\pi\Delta n L}{\lambda} = \frac{\pi n_0^3 r L V}{\lambda d} \tag{5.2}$$

For a sinusoidal modulation of the applied voltage $V(t) = V_0 \cdot \cos(\omega_m t)$ at modulation frequency ω_m, the phase modulated field is then

$$E_{PM}(t) = E_0 \mathrm{e}^{\mathrm{i}(\omega_c t + m \cdot \cos\omega_m t)} \tag{5.3}$$

where E_0 is the amplitude and ω_c the frequency of the unmodulated light field, the carrier frequency. The modulation depth m depends on the driving voltage V_0 and on a frequency dependent factor $M(\omega_m)$ [59]

$$m = \frac{\pi n_0^3 r L V_0}{\lambda d} \cdot M(\omega_m) \tag{5.4}$$

The phase modulated signal can be decomposed using Bessel functions $J_n(m)$.

$$E_{PM} = E_0 \sum_{n=-\infty}^{\infty} \mathrm{i}^n J_n(m) \mathrm{e}^{\mathrm{i}[(\omega_c + n\omega_m)t]} \tag{5.5}$$

We can see that the phase modulated output of the EOM contains the carrier field with frequency ω_c and frequency sidebands at multiples of the modulation frequency $\pm n\omega_m$. For a modulation frequency satisfying $k\omega_m = \omega_0$, where k is an integer number and ω_0 is the resonant frequency of the Raman transition there will be pairs of sidebands in the modulated beam that fulfill the resonance condition, i.e. the nth sideband together with the $(n + k)$th sideband can drive Raman transitions between the desired levels. In practice, one will choose the modulation frequency such that either the first or the second-order frequency sidebands fulfill the resonance condition with the carrier, i.e $k = 1$

[2] *Photline* NIR-MPX800-LN10

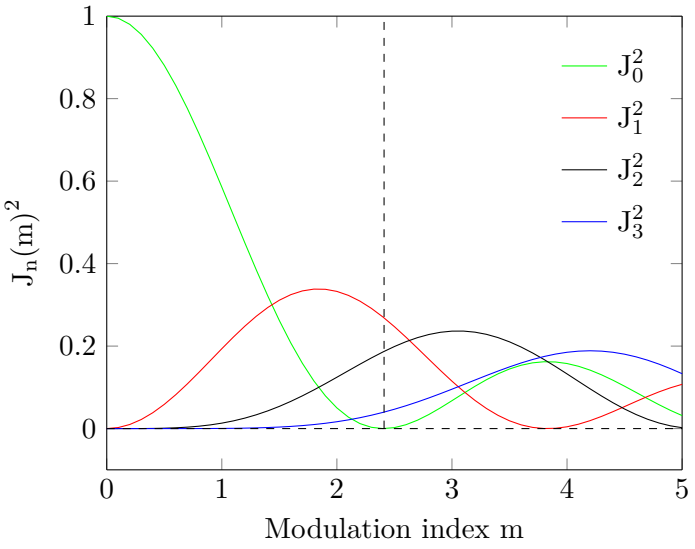

FIGURE 5.2: Squared Bessel functions. The dashed lines indicate the choice of modulation depth, $m = 2.4$ where the carrier amplitude J_0 is ideally zero.

such that $|\omega_c - \omega_m| = \omega_0$ or $k = 2$ such that $|\omega_c - 2\omega_m| = \omega_0$, as they contain most of the optical power. This is also shown in Figure 5.2.

Considering the effective coupling between the two involved levels Ω_e, which is proportional to the amplitudes of the two driving fields over the detuning as shown in chapter 2 and considering all pairs of resonant sidebands we get

$$\Omega_e \propto \frac{E_0 E_1}{\Delta} \propto \sum_{n=-\infty}^{\infty} J_n(m) J_{n+k}(m) \tag{5.6}$$

This specific sum of Bessel functions is zero for all m and k. [16, 17]. When trying to drive Raman transitions directly with the phase-modulated output of an EOM, the contributions of all resonant pairs of sidebands will destructively interfere and result in zero effective coupling.[17] It is therefore necessary to either separate the desired frequency sideband from the others, as can be done with an Mach-Zehnder interferometer as described in reference [18] or to combine the modulated beam with a second unmodulated beam.

For the combination of modulated and unmodulated beam, it is important to minimize the power in the carrier to suppress the formation of a standing light wave between the unmodulated beam at ω_c and the carrier of the modulated beam [16]. Note that for a modulation depth $m = 2.4$ the carrier amplitude ideally is zero as shown in Figure 5.2. We tested the EOM at a modulation frequency of $\omega_m = \omega_0/2 \simeq 3.415$ GHz and can suppress the power in the carrier to 5% at a driving signal input power of 21 dBm. Each of the second

frequency sidebands at $\pm 2\omega_m = \pm\omega_0$ can then drive Raman transitions together with the unmodulated carrier. Since the modulation depth is frequency dependent (Equation 5.4), it remains to be tested whether a modulation at $\omega_m = \omega_0 \simeq 6.83$ GHz is favorable, i.e yields a higher ratio of total power in the resonant sidebands to power in the carrier.

Acousto-optic modulators

We use an AOM to control the timing and pulse duration of the Raman beams. In an AOM an incoming beam is diffracted at an acoustic wave which forms a travelling grating in the modulator crystal, with a spacing given by the wavelength of the sound wave Λ. The nth order of the diffracted beam of wavelength λ comes out at an angle θ, that fulfills the Bragg condition $\sin(\theta) = n\lambda/2\Lambda$. Since the light is scattered at a moving wave, its frequency is Doppler-shifted by $\Delta\omega = n\omega_s$, where ω_s is the modulation frequency, the frequency of the acoustic wave. We implemented the AOM driven at 80 MHz modulation frequency in double-pass configuration, with a typical double-pass efficiency of 50%. The double-pass configuration is necessary for tuning the modulation frequency of the AOM without realigning the beams. By implementing a second AOM which we can modulate at a frequency detuned from the first, we have the possibility to use the system in a Bragg configuration, where we want to have the possibility to scan the modulation frequency of the AOMs.

Use as Bragg system Atoms at rest can be diffracted by a moving optical lattice created by two laser beams of different frequency. Bragg scattering has been used to probe density fluctuations of a system and to manipulate momentum states of BECs [56]. As described in chapter 2, the interaction with a light field does not only couple the atoms' internal states, but can also be used to manipulate their external states by transferring momentum onto the atoms. The transferred momentum $\mathbf{p}'$ is given by the Bragg condition $|\mathbf{p}'| = 2N\hbar k \sin(\theta/2)$, where N is the number of two-photon events and θ the angle between the wavevectors of the two light fields. For atoms with initial momentum $\mathbf{p}$, the relative frequency of the two light fields $\Delta\omega$ has to satisfy $\hbar\Delta\omega = p'^2/2m + \mathbf{p}\cdot\mathbf{p}'/m$ to couple momentum states $|\mathbf{p}\rangle \leftrightarrow |\mathbf{p}'\rangle$. In order to couple momentum states within the same internal state one therefore needs a frequency difference of the two light fields in the order of the recoil frequency ω_{rec}, as $\hbar\Delta\omega \sim p'^2/2m = \hbar^2k^2/2m = \hbar\omega_{\mathrm{rec}}$. For ^{87}Rb, the recoil frequency ω_{rec} is in the order of $\simeq 10$ kHz.

As the EOM is not suited for a modulation in this frequency range, we implement the second AOM.

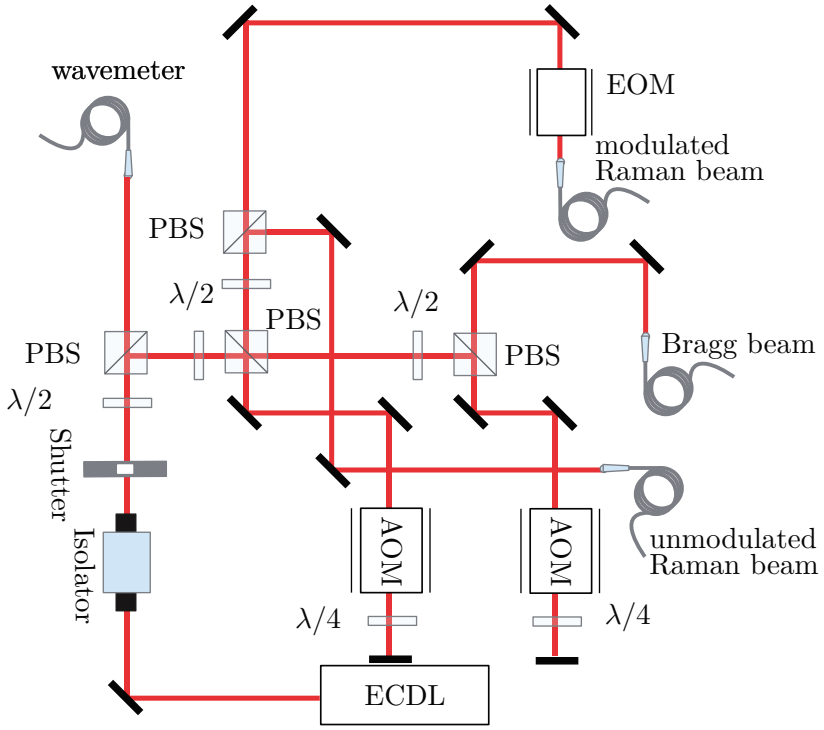

FIGURE 5.3: Optical setup to create the beams required for driving Raman transitions between the two hyperfine levels of the ^{87}Rb groundstate. An additional AOM in double pass configuration gives the possibility to drive transitions in the Bragg regime. ($\lambda/2$... *half wave plate,* $\lambda/4$... *quarter wave plate, PBS... polarizing beam splitter.*)

5.3 Implementation into Rb2

Beam geometry

The Raman beams will be guided to the viewports of the vacuum chamber with identical polarization maintaining optical fibers to ensure that the two beams have the same transverse mode. In order to get higher beam intensities at the atoms and to avoid reflections off the mirror of the atom chip, located ~ 60 μm above the atoms, we need to focus the beams. Figure 5.4 illustrates the beam geometry at the BEC: The unmodulated Raman beam shines π-polarized light with carrier frequency ω_c onto the atoms along x, perpendicular to the long axis of the BEC. It will be focused by a cylindrical lens with focal length f=500 mm such that we get an elliptical Gaussian beam with a waist $w_y = 50\mu$m along the vertical direction y and $w_z = 500\mu$m horizontally. The second, modulated Raman

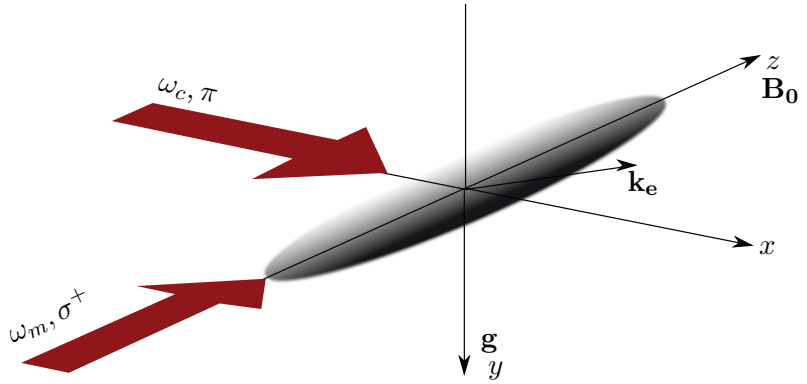

FIGURE 5.4: Sketch of proposed Raman beam geometry. The elongated BEC (grey ellipsoid) is illuminated by two Raman beams (red) perpendicular to each other. (Beam shape not realistic, for considerations concerning beam shape see text.) The net wavevector $\mathbf{k_e}$ indicates the direction of the momentum kick the output coupled atoms get.

beam illuminates the atoms along z, along the long axis of the BEC and σ^+-polarized with respect to the quantization axis defined by the magnetic field B_0 (offset or Ioffe field). We focus the beam with a cylindrical lens with focal length f=500 mm to a waist $w_x = 50\mu$m. The beam waists are therefore ~ 10 times larger than the extension of the trapped BEC, which can be estimated as $a_\perp \sim 0.25\mu$m in the transverse direction and $L \sim 25\mu$m longitudinally. This ensures that the trapped atoms are uniformly illuminated.

Expectations

Starting with an optical power of 70 mW after the optical isolator, we send ~ 65 mW into the first AOM in double pass configuration. We have a typical efficiency of 50% and have ~ 32 mW optical power to split between unmodulated and modulated Raman beams. Both beams are coupled into optical fibers with a typical insertion loss of 50%. The modulation efficiency in the resonant frequency sideband is $\sim 20\%$. As the modulated beam gets focused much stronger, we need much more power in this beam to get about the same intensities at the atoms. We propose to split the beam powers such that 24 mW go into the unmodulated beam, yielding ~ 12 mW after injection into the optical fiber, and 8 mW are sent into the EOM, yielding ~ 0.8 mW in the resonant sideband.
For the beam shaped with the cylindrical lense, we have an elliptical Gaussian intensity profile

$$I(y,z) = I_0 \cdot \mathrm{e}^{-2(y/w_y)^2} \cdot \mathrm{e}^{-2(z/w_z)^2} \tag{5.7}$$

Integration over y and z relates the total power in the beam P to the peak intensity I_0:

$$P = \int_0^\infty \int_0^\infty I(y,z)\mathrm{d}y\mathrm{d}z = I_0 \cdot w_y \cdot w_z \int_0^\infty \int_0^{2\pi} \mathrm{e}^{-2r^2} r\mathrm{d}r\mathrm{d}\varphi = \frac{\pi}{2} \cdot w_y \cdot w_z \cdot I_0$$

$$\Rightarrow I_0 = \frac{2 \cdot P}{\pi \cdot w_y \cdot w_z} \tag{5.8}$$

To get an estimate for the single photon Rabi frequency, we use the definition in Equation 2.25. The the single photon Rabi frequencies Ω_i are related to the beam intensities such that

$$\Omega = \Gamma\sqrt{\frac{I}{I_{\text{sat}}}} \tag{5.9}$$

For σ^+-polarized light the saturation intensity is $I_{\text{sat}} \sim 1.7\text{mW/cm}^2$ and for an circular beam of size $w_x = 50\mu$m with a total power of 0.8 mW yields a single photon Rabi frequency of $\Omega_0/2\pi \sim 4.7 \cdot 10^5$ kHz. For π-polarized light, the saturation intensity is $I_{\text{sat}} \sim 2.5\text{mW/cm}^2$. The unmodulated beam shaped by a cylindrical lense to a waist $w_y = 50\mu$m and $w_z = 500\mu$m with a total power of $\sim$ 12 mW also results in a Rabi frequency of $\Omega_1/2\pi \sim 4.7 \cdot 10^5$ kHz. With the detuning $\Delta \sim 100$ GHz we therefore expect a maximum two-photon Rabi frequency

$$\Omega_e = \frac{\Omega_0 \cdot \Omega_1}{2\Delta} \tag{5.10}$$

of $\Omega_e \sim 1.1$ MHz, which is three orders of magnitude higher than what we estimated for the MW coupling strength described in chapter 4. The single photon scattering rate to the first excited state is $R_{sc} \sim 30$ Hz.
This an estimate of the maximum available coupling strength. Note that the saturation intensity for circularly polarized light found in the literature [54] is for light resonant with the $|F = 2\rangle \leftrightarrow |F' = 3\rangle$ cycling transition, which is the transition that interacts strongest with light. We will operate the laser far detuned from the D2-line, therefore the saturation intensity will be higher, resulting in a lower coupling strength. Second, we cannot know the intensities at the atoms precisely. Again, we calculated with upper bounds for the beam intensities, assuming that there is no loss of beam power at the viewports of the vacuum chamber and that the beams are perfectly shaped Gaussian beams. Third, the formation of dressed states and their associated potentials (see chapter 2) can result in new bound states, which leads to a shutdown of the atom laser [16]. The practical boundary for the maximum coupling strength therefore remains to be investigated experimentally.

Photon recoil

As discussed in chapter 2, the output coupling process also transfers momentum onto the atoms. By choosing the output coupler geometry as described above, each atom undergoing a Raman transition into the untrapped $|2, 0\rangle$ state will get a momentum kick of $\mathbf{p} = \hbar\mathbf{k_e}$. As the beams are aligned perpendicular to each other and $|\mathbf{k_0}| \sim |\mathbf{k_1}| = 2\pi/\lambda = k$, this results in a momentum transfer of $\sqrt{2}\hbar k$ at 45° with respect to the long axis of the BEC in the horizontal plane. This gives the output coupled atoms an initial velocity of $v_{in} \simeq 8.3$ mm/s. We hope that this momentum kick will enable the observation of interference fringes from output coupled clouds despite the magnetic lens due to the trapping fields.

As the momentum kick brings the atoms into a region of smaller magnetic field gradients, we expect the magnetic focusing to be weaker than what we observed for clouds output coupled without momentum kick. We are planning to run GPE-simulations to check whether we can expect the output coupled atoms to form interference fringes when output coupled from a double well potential.

6 Conclusion and Outlook

In this thesis the first steps towards multiple measurements of the same ultracold system, especially probing the relative phase of a BEC confined in a double well potential, are described. The goal is to infer the relative phase from interference fringes formed by a small fraction of coherently output coupled atoms expanding in tof. Atoms from BECs confined in magnetic traps can be output coupled by coupling them to a Zeeman substate with $m_F = 0$, to an internal state which is in first order insensitive to magnetic fields.

We tested coherent output coupling with two systems integrated into the Rb2 experiment: by coupling the magnetically confined $|1, -1\rangle$ groundstate of ^{87}Rb to the $|1, 0\rangle$ state with the RF-radiation used for evaporative cooling and by output coupling to the $|2, 0\rangle$ state with radiation provided by a home-built MW-antenna.

We could not yet observe interference fringes from atoms output coupled from a double well potential, but have gained some understanding of the effects that prevent this observation: We observed a (de)focusing of the transverse profiles of the clouds coupled to the $(|1, 0\rangle)$ $|2, 0\rangle$ state compared to the transverse profiles of the clouds dropped after switching off the trap. We can attribute this to a repelling or attractive force due to the second order Zeeman shift. The force is proportional to the magnetic field gradient $\mathbf{F} \propto \pm B \nabla B$, which is strong near the chip trap. Second, we see that the transverse profiles of the output coupled clouds depend crucially on the pulse duration and frequency of the output coupling pulse, and our observations are consistent with results from other groups concerning the transverse profile of an atom laser.

Further, we built a Raman laser system, that can couple the trapped $|1, -1\rangle$ to the untrapped $|2, 0\rangle$ state with two-photon transitions. This system is ready to be integrated into the Rb2 experiment and we expect coupling strengths up to three orders of magnitude higher ($\Omega/2\pi \sim 1$ MHz) than what we can currently achieve with the MW-antenna. This gives us more flexibility in choosing the pulse duration and therefore the width of the output coupling pulse. We will direct the Raman beams perpendicular to each other onto the atoms, giving them a momentum kick of $\sqrt{2}\hbar k \simeq m \cdot 8.3$ [kg mm/s] away from the trap center, at 45° with respect to the long axis of the BEC.

On the way to observe interference fringes formed by coherently output coupled atoms we suggest to proceed with the following steps:

- Setting up a simulation for the transverse density distribution of the output coupled clouds by numerically solving the GPE. The simulation should include the effective trapping potential for ^{87}Rb atoms in the $|2,0\rangle$ and $|1,0\rangle$ state due to the second order Zeeman shift and the momentum imparted onto the atoms by the Raman laser beams. The goal of such a simulation is to find output coupler settings which allow to infer a relative phase from interference fringes formed by the output coupled cloud. We should check whether short broadband pulses or spatially selective long pulses are favorable for our purposes.
- Implementing the Raman laser beams into the Rb2 experiment as described in chapter 5, followed by a careful calibration, i.e a measurement of the coupling strength. At this point we can hopefully observe interference fringes from output coupled atoms. If not, we have to think about other ways to deal with the magnetic lens. One idea is to use RF-dressing to create a coherent superposition of the $|1,0\rangle$ and $|2,0\rangle$ state in the output coupled cloud such that the effect of the magnetic lens averages out.
- Once we can observe interference fringes from output coupled atoms we can directly use the system to study phase diffusion and the evolution of the relative phase of BECs confined in double well potentials. Further we can use the Raman system to experimentally investigate evaporative cooling in 1D systems, i.e. to study the effect of strong output coupling on the temperature of the remaining cloud [25].

In the long term, coherent output coupling may be used to study the measurement back-action on the original BEC and to realize weak measurement schemes for the relative phase of two (independent or coherently split) BECs.

Bibliography

[1] M. H. Anderson, J. R. Ensher, M. R. Matthews, C. E. Wieman, and E. A. Cornell. Observation of Bose-Einstein Condensation in a Dilute Atomic Vapor. *Science*, 269:198–201, 1995.

[2] M. R. Andrews. Observation of Interference Between Two Bose Condensates. *Science*, 275(5300):637–641, 1997.

[3] T. H. Bergeman, P. McNicholl, J. Kycia, H. Metcalf, and N. L. Balazs. Quantized motion of atoms in a quadrupole magnetostatic trap. *Journal of the Optical Society of America B*, 6(11):2249, 1989.

[4] T. Berrada. *Mach-Zehnder interferometry with interacting Bose-Einstein condensates in a double-well potential*. PhD thesis, Technische Universität Wien, 2014.

[5] T. Berrada, S. van Frank, R. Bücker, T. Schumm, J.-F. Schaff, and J. Schmiedmayer. Integrated Mach-Zehnder interferometer for Bose-Einstein condensates. *Nature communications*, 4:2077, 2013.

[6] I. Bloch, T. Hänsch, and T. Esslinger. Atom Laser with a cw Output Coupler. *Physical Review Letters*, 82(15):3008–3011, 1999.

[7] I. F. Bloch. *Atomlaser und Phasenkohärenz atomarer Bose-Einstein-Kondensate*. PhD thesis, Ludwig-Maximilians-Universität München, 2000.

[8] G. Breit and I. Rabi. Measurement of Nuclear Spin. *Physical Review*, 38(11):2082–2083, 1931.

[9] R. Bücker. *Twin-atom beam generation in a one-dimensional Bose gas*. PhD thesis, Technische Universität Wien, 2013.

[10] R. Bücker, J. Grond, S. Manz, T. Berrada, T. Betz, C. Koller, U. Hohenester, T. Schumm, A. Perrin, and J. Schmiedmayer. Twin-atom beams. *Nature Physics*, 7(8):608–611, 2011.

[11] R. Bücker, A. Perrin, S. Manz, T. Betz, C. Koller, T. Plisson, J. Rottmann, T. Schumm, and J. Schmiedmayer. Single-particle-sensitive imaging of freely propagating ultracold atoms. *New Journal of Physics*, 11(10):103039, 2009.

[12] T. Busch, M. Köhl, T. Esslinger, and K. Molmer. Transverse mode of an atom laser. *Physical Review A*, 65(4):043615, 2002.

[13] Y. Castin and J. Dalibard. Relative phase of two Bose-Einstein condensates. *Physical Review A*, 55(6):4330–4337, 1997.

[14] A. D. Cronin, J. Schmiedmayer, and D. E. Pritchard. Optics and interferometry with atoms and molecules. *Reviews of Modern Physics*, 81(3):1051–1129, 2009.

[15] K. Davis, M. Mewes, M. Andrews, N. van Druten, D. Durfee, D. Kurn, and W. Ketterle. Bose-Einstein Condensation in a Gas of Sodium Atoms. *Physical Review Letters*, 75(22):3969–3973, 1995.

[16] J. E. Debs. *The Application of Bose-Einstein Condensates to Inertial Sensing*. PhD thesis, The Australian National University, 2012.

[17] J. E. Debs, D. Döring, N. P. Robins, C. Figl, P. a. Altin, and J. D. Close. A two-state Raman coupler for coherent atom optics. *Optics Express*, 17(4):2319, 2009.

[18] I. Dotsenko, W. Alt, S. Kuhr, D. Schrader, M. Müller, Y. Miroshnychenko, V. Gomer, A. Rauschenbeutel, and D. Meschede. Application of electro-optically generated light fields for Raman spectroscopy of trapped cesium atoms. *Applied Physics B*, 78:711–717, 2004.

[19] R. Folman, P. Krüger, J. Schmiedmayer, J. Denschlag, and C. Henkel. Microscopic atom optics: From wires to an atom chip. *Advances in Atomic, Molecular and Optical Physics*, 48:263–356, 2002.

[20] C. J. Foot. *Atomic Physics*. Oxford University Press, 2005.

[21] M. Fox. *Quantum Optics An Introduction*. Oxford University Press, 2006.

[22] D. V. Freilich, D. M. Bianchi, A. M. Kaufman, T. K. Langin, and D. S. Hall. Real-Time Dynamics of Single Vortex Lines and Vortex Dipoles in a Bose-Einstein Condensate. *Science*, 329:1182–1185, 2010.

[23] J. García-Ripoll, M. Martin-Delgado, and J. Cirac. Implementation of Spin Hamiltonians in Optical Lattices. *Physical Review Letters*, 93(25):250405, 2004.

[24] I. M. Georgescu, S. Ashhab, and F. Nori. Quantum simulation. *Reviews of Modern Physics*, 86(1):153–185, 2014.

[25] P. Grisins and I. E. Mazets. Thermalization in a one-dimensional integrable system. *Physical Review A*, 84(5):053635, 2011.

[26] C. Gross, T. Zibold, E. Nicklas, J. Estève, and M. K. Oberthaler. Nonlinear atom interferometer surpasses classical precision limit. *Nature*, 464(7292):1165–9, 2010.

[27] E. W. Hagley. A Well-Collimated Quasi-Continuous Atom Laser. *Science*, 283(5408):1706–1709, 1999.

[28] R. Han, H. K. Ng, and B.-G. Englert. Raman transitions without adiabatic elimination: A simple and accurate treatment. *arXiv:1209.6569v1 [quant-ph]*, pages 1–17, 2012.

[29] S. Hofferberth, I. Lesanovsky, B. Fischer, J. Verdu, and J. Schmiedmayer. Radiofrequency-dressed-state potentials for neutral atoms. *Nature Physics*, 2(10):710–716, 2006.

[30] J. Javanainen and M. Wilkens. Phase and Phase Diffusion of a Split Bose-Einstein Condensate. *Physical Review Letters*, 78(25):23–26, 1997.

[31] M. Kasevich, D. S. Weiss, E. Riis, K. Moler, S. Kasapi, and S. Chu. Atomic Velocity Selection Using Stimulated Raman Transitions. *Physical Review Letters*, 66(18):2297–2300, 1991.

[32] W. Ketterle, D. Durfee, and D. Stamper. Making, probing and understanding Bose-Einstein condensates. In *Enrico Fermi summer school on Bose-Einstein condensation*, Varenna, 1999.

[33] M. Köhl, T. Busch, K. Molmer, T. Hänsch, and T. Esslinger. Observing the profile of an atom laser beam. *Physical Review A*, 72(6):063618, 2005.

[34] C. Koller. *Towards the experimental realization of Hybrid Quantum Systems*. PhD thesis, 2012.

[35] R. Loudon. *The Quantum Theory of Light*. Oxford Science Publications, Oxford, 3 edition, 2000.

[36] H. J. Metcalf and P. van der Straten. *Laser Cooling and Trapping*. Springer-Verlag, New York, 1999.

[37] M.-O. Mewes, M. R. Andrews, D. M. Kurn, D. S. Durfee, C. G. Townsend, and W. Ketterle. Output Coupler for Bose-Einstein Condensed Atoms. *Physical Review Letters*, 78(4):582–585, 1997.

[38] E. Nicklas. *Setup and Test of a Raman Laser System*. Diploma thesis, University of Heidelberg, 2008.

[39] A. Öttl, S. Ritter, M. Köhl, and T. Esslinger. Hybrid apparatus for Bose-Einstein condensation and cavity quantum electrodynamics: Single atom detection in quantum degenerate gases. *Review of Scientific Instruments*, 77(6):063118, 2006.

[40] H. Perrin. Adiabatic potentials. Lecture Notes, Les Houches, 2013.

[41] H. Perrin. Laser cooling and trapping. Lecture Notes, Les Houches PreDocSchool, 2014.

[42] C. Pethick and H. Smith. *Bose-Einstein Condensation in Dilute Gases*. Number 1991. Cambridge University Press, 2 edition, 2008.

[43] W. D. Phillips. Nobel Lecture: Laser cooling and trapping of neutral atoms. *Reviews of Modern Physics*, 70(3):721–741, 1998.

[44] T. Plisson. *Coherent Manipulation of Bose-Einstein Condensates with Microwave and Radio Frequency Fields*. Diploma thesis, Wien, 2009.

[45] J. Ringot, Y. Lecoq, J. C. Garreau, and P. Szriftgiser. Generation of phase-coherent laser beams for Raman spectroscopy and cooling by direct current modulation. *The European Physical Journal D*, 7:285–288, 1999.

[46] J.-F. Riou, W. Guerin, Y. Coq, M. Fauquembergue, V. Josse, P. Bouyer, and A. Aspect. Beam Quality of a Nonideal Atom Laser. *Physical Review Letters*, 96(7):070404, 2006.

[47] N. P. Robins, P. A. Altin, J. E. Debs, and J. D. Close. Atom lasers: production, properties and prospects for precision inertial measurement. *arXiv:1209.2172 [cond-mat.quant-gas]*, 2012.

[48] W. Rohringer. *Dynamics of One-Dimensional Bose Gases in Time-Dependent Traps*. PhD thesis, Technische Universität Wien, 2014.

[49] M. Saba, T. A. Pasquini, C. Scanner, Y. Shin, W. Ketterle, and D. E. Pritchard. Light Scattering to Determine the Relative Phase of Two Bose-Einstein Condensates. *Science*, 307:1945–1948, 2005.

[50] J. Sakurai and J. Napolitano. *Modern Quantum Mechanics*. Addison-Wesley, San Francisco, 2 edition, 2011.

[51] T. Schumm. *Bose-Einstein condensates in magnetic double well potentials*. Phd, Universite Paris 11, 2005.

[52] T. Schumm, S. Hofferberth, L. M. Andersson, S. Wildermuth, S. Groth, I. Bar-Joseph, J. Schmiedmayer, and P. Krüger. Matter-wave interferometry in a double well on an atom chip. *Nature Physics*, 1(1):57–62, 2005.

[53] B. W. Shore. *The Theory of Coherent Atomic Excitation Volume 2: Multilevel Atoms and Incoherence*. John Wiley & Sons, 1990.

[54] D. A. Steck. Rubidium 87 D Line Data, 2010.

[55] D. A. Steck. Quantum and Atom Optics, 2014.

[56] J. Stenger, S. Inouye, A. P. Chikkatur, D. E. Pritchard, and W. Ketterle. Bragg Spectroscopy of a Bose-Einstein Condensate. *Physical Review Letters*, 82(23):4569–4573, 1999.

[57] J. Struck, M. Weinberg, C. Ölschläger, P. Windpassinger, J. Simonet, K. Sengstock, R. Höppner, P. Hauke, A. Eckardt, M. Lewenstein, and L. Mathey. Engineering Ising-XY spin-models in a triangular lattice using tunable artificial gauge fields. *Nature Physics*, 9(11):738–743, 2013.

[58] G. Tackmann, M. Gilowski, C. Schubert, P. Berg, T. Wendrich, W. Ertmer, and E. M. Rasel. Phase-locking of two self-seeded tapered amplifier lasers. *Optics express*, 18(9):9258–65, 2010.

[59] P. Technologies. Spectral analysis of the rf phase modulation of an optical signal. Application Note.

[60] M. Trinker, S. Groth, S. Haslinger, S. Manz, T. Betz, S. Schneider, I. Bar-Joseph, T. Schumm, and J. Schmiedmayer. Multilayer atom chips for versatile atom micromanipulation. *Applied Physics Letters*, 92(25):254102, 2008.

[61] S. van Frank, A. Negretti, T. Berrada, R. Bücker, S. Montangero, J.-F. Schaff, T. Schumm, T. Calarco, and J. Schmiedmayer. Interferometry with non-classical motional states of a Bose-Einstein condensate. *Nature communications*, 5:4009, 2014.

[62] S. Wildermuth, P. Krüger, C. Becker, M. Brajdic, S. Haupt, A. Kasper, R. Folman, and J. Schmiedmayer. Optimized magneto-optical trap for experiments with ultracold atoms near surfaces. *Physical Review A*, 69(3):030901, 2004.

[63] W. H. Wing. On neutral particle trapping in quasistatic electromagnetic fields. *Progress in Quantum Electronics*, 8(3-4):181–199, 1984.

[64] T. Zanon-Willette, E. de Clercq, and E. Arimondo. Magic Radio-Frequency Dressing of Nuclear Spins in High-Accuracy Optical Clocks. *Physical Review Letters*, 109(22):223003, 2012.

[65] N. Zettili. *Quantum Mechanics: Concepts and Applications*. John Wiley & Sons, Chichester, 2 edition, 2009.

Acknowledgments

I would like to thank Jörg Schmiedmayer for giving me the opportunity to start a master thesis in his group. RuGway Wu was a great and patient advisor. The atomchip group and the Rb2 team - Marie Bonneau, Tarik Berrada, Marine Pigneur, Sandrine van Frank and RuGway Wu - provided a stimulating and supporting working environment, I am looking forward to continue to work in this group. And thanks to Thorsten Schumm for sparking my motivation to play with atoms and lasers as well as providing support whenever needed.

I also wish to thank my family - Andreas, Dietlind, Eva, Ines, Ruth and Yeliz - for their support and interest in what I'm doing; Pauli for these first years of physics together; Lukas; and Eva for knowing about BECs - Ja dann wollens kuscheln, wenns kalt is - and so much more.

CV Mira Maiwöger
mira.maiwoeger@ati.ac.at

Education

12/2013–04/2015 Master Thesis in Prof. Jörg Schmiedmayer's group at the Atominstitut Vienna

10/2014 Acceptance to CoQuS doctoral program

02/2013–07/2013 Erasmus exchange at Boğaziçi University in Istanbul

11/2011–04/2015 Master student in Physics at the University of Vienna and at the Technical University of Vienna

10/2007–11/2011 BSc. in Physics at the University of Vienna

09/1998–06/2006 Highschool: Bundesrealgymnasium Steyr Michaelerplatz (mathematical and scientific focus)

Conference visits

Sept 15–26, 2014 Les Houches ColdAtoms PreDoc School *Ultracold Atoms and Precision Measurements*. (Poster title: *Raman Outcoupler for an Ultracold Atoms Experiment*)

19-22/06/2014 Quantum [Un]Speakables II: 50 Years of Bell's Theorem

7-9/09/2011 'Interferometric Investigations of Physical Knowledges and Gender in the Making', Symposium in Uppsala, Sweden

2-5/06/2011 CEQIP (Central European Quantum Information Processing) 2011

Working experience

10/2011–12/2013 (Winter terms) Tutor at the Institute of Physics, University of Vienna (Course: *Introduction to mathematical Methods of Physics*, Prof. Christoph Dellago)

11/2011–02/2013 Referent for FIT (Frauen in die Technik) in Vienna

09/2006–07/2007 Nanny in Paris, France

Languages

German - native
English - fluent
French - proficient
Turkish - conversant
Spanish - basic